Additive manufacturing of Ti–6Al–4V parts through laser metal deposition (LMD)

Process, microstructure, and mechanical properties

Azarniya, Abolfazl; Colera, Xabier Garmendia; Mirzaali, Mohammad J.; Sovizi, Saeed; Bartolomeu, Flavio; St Weglowski, Mare k.; Wits, Wessel W.; Yap, Chor Yen; Ahn, Joseph; Miranda, Georgina

DOI
10.1016/j.jallcom.2019.04.255

Publication date
2019

Document Version
Final published version

Published in
Journal of Alloys and Compounds

Journal of Alloys and Compounds 804 (2019) 163–191

Contents lists available at ScienceDirect

Journal of Alloys and Compounds

journal homepage: http://www.elsevier.com/locate/jalcom

Review

Additive manufacturing of Ti–6Al–4V parts through laser metal deposition (LMD): Process, microstructure, and mechanical properties

Abolfazl Azarniya [a, i, *], Xabier Garmendia Colera [b], Mohammad J. Mirzaali [c], Saeed Sovizi [a], Flavio Bartolomeu [d], Mare,k St Weglowski [e], Wessel W. Wits [f], Chor Yen Yap [g], Joseph Ahn [h], Georgina Miranda [d], Filipe Samuel Silva [d], Hamid Reza Madaah Hosseini [a], Seeram Ramakrishna [i, **], Amir A. Zadpoor [c]

[a] Materials Science and Engineering Department, Sharif University of Technology, P.O. Box 11155-9466, Azadi Avenue, Tehran, Iran
[b] Centre for Materials and Structures, School of Engineering, University of Liverpool, L69 3GH, United Kingdom
[c] Department of Biomechanical Engineering, Faculty of Mechanical, Maritime, and Materials Engineering, Delft University of Technology (TU Delft), Mekelweg 2, 2628 CD, Delft, the Netherlands
[d] Center for Micro-Electro Mechanical Systems (CMEMS-UMinho), University of Minho, Campus de Azurém, 4800-058 Guimarães, Portugal
[e] Department of the Testing of Materials Weldability and Welded Construction, Lukasiewicz Research Network - Institute of Welding, Bl. Czeslawa 16-18, Gliwice 44-100, Poland
[f] Mechanical & Electrical Engineering, THALES Netherlands, P.O. Box 42, 7550 GD Hengelo, Netherlands
[g] Divergent Technologies Inc., Los Angeles, USA
[h] Department of Mechanical Engineering, Imperial College London, South Kensington Campus, London, SW7 2AZ, UK
[i] Department of Mechanical Engineering, National University of Singapore, 9 Engineering Drive 1, Singapore 117576, Singapore

ARTICLE INFO

Article history:
Received 21 September 2018
Received in revised form
20 April 2019
Accepted 23 April 2019
Available online 11 May 2019

Keywords:
Laser metal deposition
Additive manufacturing
Ti–6Al–4V
Microstructure
High performance titanium alloys
Mechanical properties

ABSTRACT

As one of the most important additive manufacturing (AM) techniques, laser metal deposition (LMD) has been extensively studied specially during the last few years. Similar to other AM techniques, the quality of LMD parts is highly dependent on the processing parameters that need to be optimized so as to obtain geometrically accurate parts as well as favorable microstructures and, thus, mechanical properties. The present review paper therefore aims to present a critical analysis and overview of the relationship between processing parameters, microstructure, and mechanical properties of LMD components made from the Ti–6Al–4V alloy. Moreover, we discuss the applications of LMD parts in the aerospace and biomedical industries as well as the potential of LMD techniques for fabrication of more complex parts such as cellular structures. The paper concludes with a summary of the most important findings and suggestions for future research.

Contents

* Corresponding author. Materials Science and Engineering Department, Sharif University of Technology, P.O. Box 11155-9466, Azadi Avenue, Tehran, Iran.
** Corresponding author.
E-mail addresses: abolfazl.azarniya@u.nus.edu.sg (A. Azarniya), xabier.garmendia@liverpool.ac.uk (X.G. Colera), m.j.mirzaalimazandarani@tudelft.nl (M.J. Mirzaali), Sovizi71@gmail.com (S. Sovizi), flaviojorgebartolomeu@gmail.com (F. Bartolomeu), marek.weglowski@is.gliwice.pl (M. St Weglowski), w.w.wits@utwente.nl (W.W. Wits), cyap001@e.ntu.edu.sg (C.Y. Yap), joseph.ahn08@imperial.ac.uk (J. Ahn), gmiranda@dem.uminho.pt (G. Miranda), fsamuel@dem.uminho.pt (F.S. Silva), madaah@sharif.edu (H.R. Madaah Hosseini), seeram@nus.edu.sg (S. Ramakrishna), a.a.zadpoor@tudelft.nl (A.A. Zadpoor).

https://doi.org/10.1016/j.jallcom.2019.04.255
0925-8388/

Nomenclature

3D	Three Dimensional
AM	Additive Manufacturing
BCC	Body Centered Cubic
CAD	Computer-Aided Design
DED	Directed Energy Deposition
DLD	Direct Laser Deposition
DLF	Directed Light Fabrication
DMD	Direct Metal Deposition
DMLS	Direct Metal Laser Sintering
EBM	Electron Beam Melting
FCGR	Fatigue Crack Growth Rate
FEA	Finite Element Analysis
FEM	Finite Element Modeling
GA	Gas Atomization
HAZ	Heat Affected Zones
HCF	High Cycle Fatigue
HCP	Hexagonal Closed Packed
HIP	Hot Isostatic Pressing
LBM	Laser Beam Melting
LCF	Low Cycle Fatigue
LENS	Laser Engineered Net Shaping
LMD	Laser Metal Deposition
PBF	Powder Bed Fusion
PREP	Plasma Rotating Electrode
SLM	Selective Laser Melting
SLS	Selective Laser Sintering
SMD	Shape Metal Deposition
STL	Standard Tessellation Language
WAAM	Wire + Arc Additive Manufacturing

1. Introduction

In recent years, the fabrication of three-dimensional (3D) components through additive manufacturing (AM) has been widely studied and attracted the attention of various industries worldwide [1,2]. In accordance with ISO 17296–2:2015 (*Additive manufacturing, general principles, overview of process categories, and feedstock)* [3], AM techniques can be classified into seven categories (Fig. 1). These categories include VAT photopolymerisation, material jetting, binder jetting, sheet lamination, material extrusion, powder bed fusion (PBF), and directed energy deposition (DED). PBF and DED are the most frequently used AM techniques for fabrication of Ti–6Al–4V parts particularly those aimed for application in biomedical and aerospace industries.

PBF comprises techniques in which an energy source (*i.e.*, laser beam or electron beam) is used to melt and fuse the powder residing in a powder bed [4]. Various energy sources require different atmospheres. In general, nitrogen or argon gas is required for laser systems, while vacuum is preferred when using an electron beam. For building each slice of the 3D shape, a new layer of powder is spread over the build plate [5], and is then selectively melted by the energy source. Subsequently, the build platform is lowered and another layer of powder is deposited on top of the previous ones. This procedure is repeated until all the layers

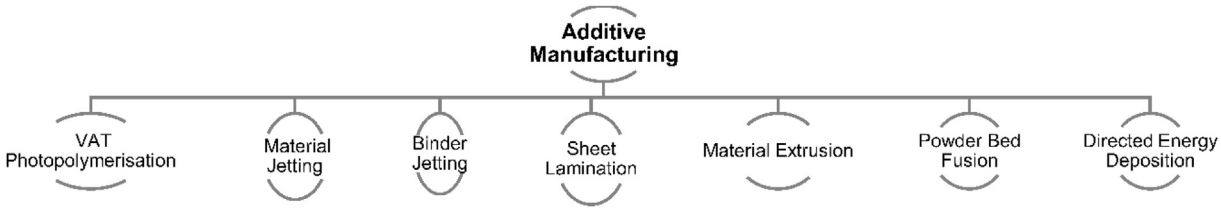

Fig. 1. The classification of AM techniques according to ISO 17296–2:2015 [3].

resulting from the slicing of the geometry defined by a computer-aided design (CAD) file are built.

In DED, however, the deposition and fusing of the fed material occurs quasi-simultaneously using an energy source such as laser, electron beam, or plasma arc [5]. The material (*i.e.*, wire, powder, or strip) is deposited on the substrate from a nozzle mounted on a multi-axis arm. Similar to other AM techniques, the fabrication process is layer-by-layer and is performed according to a pre-planned scanning trajectory [2,6].

Among PBF and DED techniques, the most popular ones for the fabrication of metallic parts are as follows:

- Laser beam melting (LBM) [7,8] – (*PBF category*);
- Electron beam melting (EBM) [9] – (*PBF category*);
- Laser metal deposition (LMD) [2,10,11]– (*DED category*).

Although several standard terminologies for these techniques are suggested in the scientific and technical literature, manufacturers often adopt their own terminologies. Table 1 introduces these terminologies and classifies them into two large groups. Based on this classification, the main AM techniques for metallic materials include LBM, EBM, and LMD.

LMD processes offer a number of unique advantages over other AM techniques particularly when a near-net-shape is desired. For example, large parts that do not fit in the build volume of PBF processes could be processed with LMD techniques. Moreover, LMD techniques are highly efficient for the repair of damaged or worn-out parts or when new features need to be added to already existing parts [12,13]. The ability to fabricate functionally graded materials, higher deposition rates, and a more comprehensive processing window for the optimization of finished parts are some other advantages of this manufacturing process [14].

AM techniques enable the fabrication of parts directly from a 3D model [15]. This capability together with the form-freedom and material choice freedom offered by AM has triggered new and revolutionary approaches in engineering design [16]. The versatility of AM techniques contrasts with the limitations that conventional processing routes such as casting, forging, and machining suffer from Ref. [17]. For the fabrication of Ti–6Al–4V parts, for example, the conventional processing routes often result in high material wastage [7,9] while requiring expensive customized dies, forming tools, molds [18], and finishing operations as well as all other difficulties reactivity of Ti–6Al–4V (*i.e.,* oxidation and decomposition problems). On the contrary, AM resulting from the high techniques allow for the fabrication of Ti–6Al–4V near-net-shape products with complex geometries while reducing the environmental impact and increasing the production sustainability [18]. The huge potential of AM processes has therefore been used in the production of custom-made solutions, especially for high-added-value products of automotive, aerospace, aeronautics, and biomedical industries [5,19].

2. Ti–6Al–4V

Ti–6Al–4V is one of the most popular and commercially available titanium alloys [20,21]. Its microstructure contains a mixture of α-phase with a hexagonal closed packed (HCP) crystal structure and β-phase with a body centered cubic (BCC) structure. When rapidly cooled down from high temperatures, the β phase can transform into a martensitic α phase with a HCP crystal structure and a $P6_3/mmc$ space group [22]. This Ti–Al–V system contains 6 wt% aluminum as α-stabilizer and 4 wt% vanadium as β-stabilizer [2]. The HCP crystal structure is stable at the room temperature and transforms to a BCC structure at the β-transus temperature (from ≈995 to >1000 °C depending on the Al and O contents) [23].

A variety of processing routes and post-AM heat treatments have been developed to adjust the microstructure of AM Ti–6Al–4V and manipulate the distribution, morphology, and size of α and β phases. These changes are highly correlated to the cooling rate that is applied when the alloy is cooled down starting from temperatures above the β-transus temperature [24]. The microstructure of the Ti6AL4V alloy is very sensitive to the thermal

Table 1
The AM techniques commonly used for metals and their alternative names.

ISO category	Terminology used in this article	Terminology	Refs.
Powder Bed Fusion (PBF)	Laser Beam Melting (LBM) and Electron Beam Melting (EBM)	Laser Beam Melting (LBM)	[7]
		Selective Laser Melting (SLM)	[15,37]
		Selective Laser Sintering (SLS)	[248]
		Electron Beam Melting	[9,249]
		Direct Metal Laser Sintering (DMLS)	[1]
		LaserCUSING	[250]
		Industrial 3D printing	[251]
Directed Energy Deposition (DED)	Laser Metal Deposition (LMD)	Laser Metal Deposition (LMD)	[2,11]
		Direct Laser Deposition (DLD)	[42]
		Laser Engineered Net Shaping (LENS)	[77]
		Direct Metal Deposition (DMD)	[252]
		Laser Cladding	[39]
		Directed Light Fabrication (DLF)	[253]
		Shape Metal Deposition (SMD)	[21]

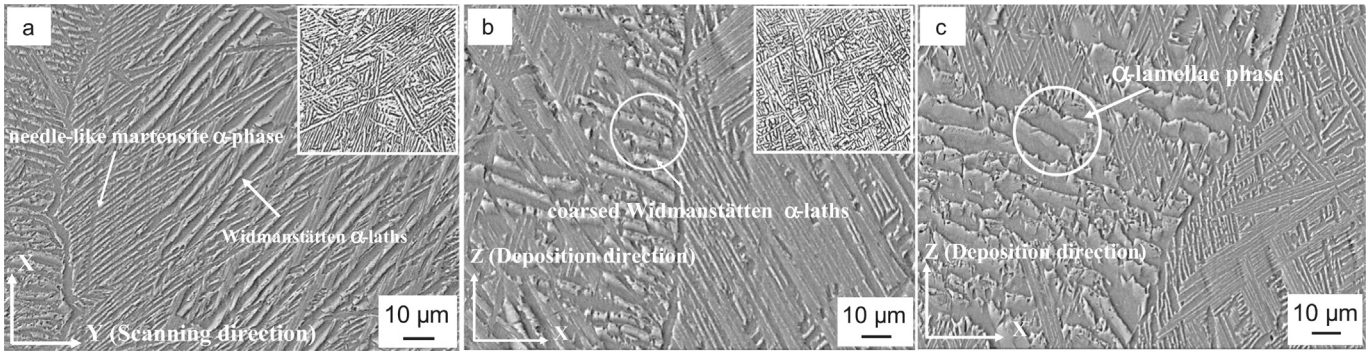

Fig. 2. The microstructural characteristics of Ti–6Al–4V parts produced by LMD: (a) *x*–*y* surface and (b–c) *x*–*z* surface (reproduced from Ref. [30]).

history and can mainly evolve in the form of fully lamellar homogenous large β grains, bi-modal with smaller α colony sizes, or equiaxed α-β microstructures [25–27]. In LMD components, the lamellar microstructure is commonplace and will be broadly addressed in the present review.

When the cooling rate is slow (*i.e.*, <20 °C/s), nucleation and growth processes occur and form α Widmanstätten laths within the β matrix [24]. These microstructures are usually observed in conventional wrought and cast materials. For cooling rates between 20 and 410 °C/s, the length and thickness of α-lamellae decrease, thereby enhancing the mechanical strength [17]. If the cooling rate is high enough (*i.e.*, >410 °C/s), the β-phase undergoes a diffusionless transformation to martensitic α′-phase [10,24]. One of the most important challenges when using AM processes is to fabricate highly dense parts with relative densities higher than 99.5%. However, the manufacturing defects occurring during the AM process can result in parts with lower densities. These defects can present themselves in the form of micro-porosities (*i.e.*, <50 μm) that facilitate the propagation of cracks and diminish the mechanical properties of AM Ti–6Al–4V [28,29].

When producing Ti–6Al–4V parts using LMD, several processing parameters play important roles in affecting the microstructure-sensitive properties of the material. It has been shown that the final microstructure of Ti–6Al–4V significantly affects its strength, ductility, hardness, toughness, fatigue, wear resistance, and corrosion behavior. A typical example of these microstructures is presented in Fig. 2. As is clear from this figure, the prior-β columnar grains grow epitaxially along the deposition direction. The original β grains are decorated with a grain boundary α phase [30,31]. The microstructure of LMD Ti–6Al–4V parts consists of β grains, a sequence of needle-like martensitic α-phase, a large amount of Widmanstätten α-laths structures, and a few β-phase between the α-laths [30].

Ti–6Al–4V is considered the workhorse titanium alloy in multiple industrial sectors. High strength [32], low weight ratio [33], superior corrosion resistance [19], and high-temperature performance [34,35] are the main characteristics that make this material suitable for a diversified range of high added value products. Transport and automotive [24], chemical, oil and gas extraction, sports, electronics, aerospace [2,10,36] and medical device (*e.g.*, orthopaedic and dental implants) industries [32,37] are some examples of a wide range of the areas where Ti–6Al–4V is applied. As compared to cobalt-chromium alloys and stainless steels used in medical devices, Ti–6Al–4V presents 50% lower Young's modulus (around 110 GPa) [38], 50% lower weight, outstanding corrosion resistance [39], and high levels of biocompatibility [40,41]. These advantages make this alloy appealing for the fabrication of medical devices such as orthopaedic and dental implants [6]. Ti–6Al–4V is also an appropriate material for aerospace products such as airframes, flaps, and engine mountings [2], as its use represents significant volume reduction and weight saving as compared to the commonly used steels and aluminum alloys. Moreover, Ti–6Al–4V exhibit high levels of fatigue resistance and high-temperature mechanical properties [42]. The superior properties of AM Ti–6Al–4V processed by AM techniques have allowed for the development of innovative engineering solutions that could potentially improve the quality of our lives through customized and more efficient medical devices as well as through improved sustainability and reduced environmental footprint of industrial products.

There are some technical reports confirming that LMD is superior to some traditional manufacturing methods in terms of

Table 2
A short list of the experimental results regarding the mechanical properties of Ti–6Al–4V components manufactured by LMD and comparing them with those of the materials fabricated using traditional manufacturing techniques.

Fabrication method and post treatments	Yield stress (MPa)	UTS (MPa)	Elongation at failure	Hardness (HV)	Ref.
Casting and post heat treatments at 800-1100 °C	–	1100–14000	1.2–4%	360–425	[254]
Casting	999	1173	6%	–	[255]
Casting and HIP	833.9	900.2	6%	325	[256]
Centrifugal casting	898	981	3%	378	[257]
HIP	851	932	16.2%	–	[258]
Hydrogen sintering and phase transformation (HSPT)	930–974	994–1024	13.8–17.8%	–	[259]
Forging and recrystallization	711	876	12.4%	–	[260]
LMD	–	900–1000	–	326–392	[50]
LMD	871–1015	995–1118	18%	–	[123]
LMD	697–884	790–960	5–12%	–	[55]
LMD	–	1014–1085	9.2–13.3%	390	[79]
LMD	–	1060	14%	–	[122]

fabricating materials with enhanced mechanical properties. Table 2 present a brief list of the experimental results reported to date and compares the mechanical properties of LMD Ti–6Al–4V components with those fabrciated using traditional manufacturing techniques. As is clear from this table, the mechanical properties of Ti–6Al–4V parts strongly depend on the fabrication method as well as the applied post-manufacturing heat treatments and thermal history. Moreover, it can be seen that LMD Ti–6Al–4V components benefit from a good balance between the mechanical strength and ductility when compared to those made through other manufacturing techniques.

3. Scope of the present study

In this paper, we review LMD techniques with a focus on the Ti–6Al–4V parts that are aimed for application in the biomedical and aerospace industries. In particular, we thoroughly discuss the physicomechanical properties of LMD Ti–6Al–4V components and explore the phase transformations and their influence on the resulting properties.

A number of review articles have been published before about the LMD technology and some of its important aspects for different metals and alloys. For example, Thompson et al. have in 2015 broadly reviewed the LMD-based fabrication of different metals and alloys including the relevant transport phenomena, modeling aspects [43], optimization of processing parameters, and mechanical behavior [31]. In particular, they had focused on the processing parameters and transport phenomena and their influence on the mechanical properties of metallic systems such as titanium alloys, steels, and super-alloys. In 2015, Bian et al. [31] published a short review article briefly addressing LMD Ti–6Al–4V. Although that paper covers certain interesting aspects of LMD Ti–6Al–4V, it does not cover a large number of recent studies that have appeared since 2015. Given that many studies on LMD Ti–6Al–4V have been published since then, there is an urgent need for a review paper that covers the new results and deals with the principles of LMD and their application for obtaining highly dense parts made from Ti–6Al–4V. This paper aims to fill that gap and inform readers who would like to start LMD-related research while updating those who are already involved in this line of scientific inquiry with the latest developments in this area. We start off by introducing the main concepts of LMD, the types of microstructures resulting from it, the relevant physical phenomena, and the processing parameters and how they influence the physicomechanical properties of the resulting parts. In the second step, a comprehensive overview of the critical experimental results and recently published reports on LMD Ti–6Al–4V is presented. We also highlight the existing challenges and opportunities in this active and exciting area of research.

4. Laser metal deposition

4.1. Introduction

Driven by the private industry, the early concepts of direct laser deposition (DLD) emerged in 1980s, as evidenced by a patent from Brown et al. [44] describing layer-wise additive deposition working on the basis of powder (or wire) metallurgy. In 1988, Mehta et al. [45] patented a technique for the repair of metallic components that combined a laser beam with blown powder. In the same year, Hammeke [46] patented a laser spray nozzle technology while Buongiorno [47] patented a metal cladding nozzle a few years later in 1994. Similarly, directed light fabrication (DLF) was proposed as a form of single-nozzle powder-based DLD by Lewis et al. [48] in the mid-1990s at Los Alamos National Laboratory. In the mid-to-late 1990s, researchers at Sandia National Laboratories innovated and trademarked the process as laser engineered net shaping (LENS®), which deployed multiple nozzles for the powder delivery. After 1997, the company "Optomec" started to commercialize the LENS® technology [31]. A new generation of these technologies are currently being developed by several companies under the generic name of LMD.

The first step for the production of a component using LMD is the preparation of a computer-generated 3D model of the desired part that is often made using a computer aided design (CAD) program. The CAD geometry is then sliced into parallel thin layers that are perpendicular to a selected build direction and is exported in a widely accepted file format such as the standard tessellation language (STL). Finally, this file is imported into the computer controlling the LMD machine to build the part. In LMD, the feed material (in the form of wire or powder) and energy are delivered simultaneously to a given location. At this (moving) location, the delivered (laser) energy melts the feed material to form a melt pool. In the case of powder-based LMD, the powder is blown to the melt pool coaxially to the energy beam while the cladding head moves in the x-y plane, creating a track of solidified material. After all tracks are completed in the x-y plane, the cladding nozzle is elevated along the z-axis to start the deposition of the subsequent layer. Before starting the deposition of the first track, the surface of the substrate plate should be cleaned with ethanol [49]. Fig. 3 presents a schematic illustration of the LMD process and its setup.

In the aerospace industry, a commonly used parameter is the buy-to-fly ratio, which is defined as the ratio of the weight of the raw material used for a component to its final weight. AM technologies such as LMD dramatically reduce this ratio and serve as an interesting business opportunity for the fabrication of small- and medium-sized Ti–6Al–4V parts [50].

LMD can be applied for preventive and corrective maintenance of critical parts in which case its name is often changed to "laser cladding" [51,52]. Moreover, LMD could be used to address the machining errors and last-minute engineering redesigns that ordinarily lead to long lead times and extra costs. As compared to conventional repair technologies such as tungsten inert gas or gas metal arc welding, LMD allows for material deposition with multiple advantages including a low heat input that minimizes the distortion and the thermal damage of the existing substrate. Furthermore, finer microstructures can be obtained using this repeatable and automatable process [51].

Currently, there are only a limited number of LMD commercial machine manufacturers. Many of the end users of LMD therefore design and integrate the components required for a LMD cell

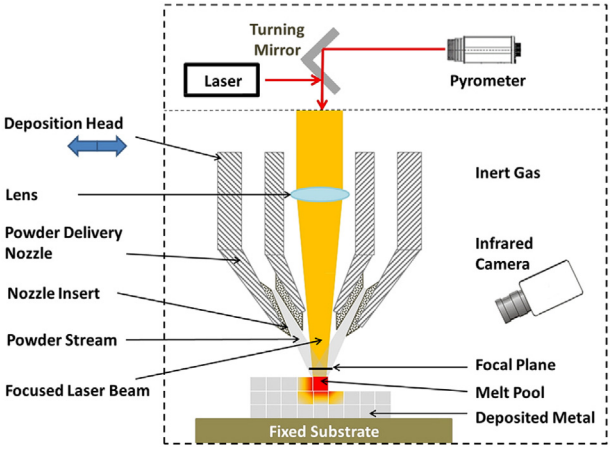

Fig. 3. A schematic representation of the powder-blown LMD setup [43].

Table 3
The relative porosity of the powder materials made by GA and PREP [49].

Sample	Powder volume (mm^3)	Pores volume (mm^3)	% Porosity
GA	3.877	0.002117	0.055
PREP	2.329	0.000399	0.017

themselves. These components usually include a laser source, a fiber/wire/powder feeder, a robot and/or an axis-controlled table, a cooling system, optical lenses, and a cladding head or nozzle. The type of lasers and their wavelengths vary between different LMD machines. However, fiber, CO_2, or Nd:YAG lasers with powers in the range of 1 and 5 kW [31] are used in most cases. In LMD machines, the generated laser beam is transported to the cladding head using a fiber. The beam is then collimated and re-oriented using different optical devices such as collimators or 45° mirrors [31]. The angle, rate, and location of the blown powder can strongly affect the deposition process. The powder is usually fed using a volumetric feeding device utilizing argon gas for carrying the powder through a hose to the nozzle powder channels. Six-axis robots with coupled cladding nozzles are usually employed in the LMD process to increase the process flexibility. When fabricating components that require the generation of circular paths, the substrate can be moved using precise x-y gantries [53]. Nozzles usually have 3 to 4 equally spaced orifices that are directed towards the focus point of the laser beam. LMD nozzles should be carefully designed so as to prevent the nozzle orifices from clogging. Furthermore, it is important to keep the nozzles cooled to prevent possible deformations in the cladding head. The cladding head is usually equipped with a pyrometer or an infrared camera to monitor the temperature of the melt pool.

The chemical composition, physical properties (*e.g.*, flowability), and morphology of the starting powder can influence the roughness and geometrical accuracy of the final part as well as the melt pool behavior. Most of the powder material used in LMD is made through gas-atomization (GA) with particle sizes that range between 10 and 100 μm [54. GA has the disadvantage of occasionally entrapping gas bubbles in the generated powder given its rapid solidification process. In this process, the molten metal passes into a nozzle through a ceramic feed tube. The gas stream strikes the melt as it emerges from the melt nozzle, resulting in spherically shaped metal powder [54]. However, the alternative technique of plasma rotating electrode (PREP) has been found to result in better sphericity and less initial porosity (Table 3) [49]. In general, the size distributions of the powder particles produced through GA and PREP are remarkably different. In a case study, for example, the mean size of the particles made through GA was 94 μm, while it was 72 μm for the ones made by PREP [49]. Fig. 4 shows the rough surfaces, satellite particles, and surface pores of GA Ti–6Al–4V particles. The initial powder shape, size, and defects are found to strongly influence the surface roughness, deposited track thickness, intralayer porosity, and the hardness of the final LMD parts [49].

The processing parameters are the other factors strongly affecting the microstructure and mechanical properties of LMD Ti–6Al–4V parts. Among these parameters, the laser power, nozzle speed, (powder or wire) feed rate, laser spot diameter, hatch interspacing, deposition strategy, substrate temperature, powder shape, and powder size are the most important parameters [31]. The feed rate is the average mass of the feedstock leaving the nozzle per minute and ranges between 1 and 10 g/min [31]. The inclination of the deposition nozzle with respect to the substrate has to be taken into consideration, because high inclination angles can bring powder feeding rates below the desired levels. In addition, non-coaxial alignment of the powder stream with the focus spot of the laser beam can result in geometrical inaccuracies [31].

The type of the deposition strategy or deposition pattern is another factor influencing the width and height of the LMD-deposited tracks [31]. The selection of an adequate scan pattern may reduce the amount of residual stresses and thermal distortions [31]. In general, there are four common deposition patterns including raster, bi-directional, offset, and fractal [31]. It has been shown that the geometrical accuracy can be achieved with lower deposition rates, giving rise to longer production times [31]. Among the deposition strategies, the circle and spiral strategies avoid the resolution problem in cylindrical parts. Fabrication of smaller circles is, however, challenging due to the accumulation of significant amount of heat in a small area. In addition, the acceleration of the nozzle in small circles is very high, which can adversely affect the accuracy of the nozzle movements.

Among the main advantages of LMD, the material cost saving is of great significance and is particularly appreciated by the automotive and aerospace industries, where a weight reduction can have a remarkable economic impact [55]. The current manufacturing techniques used in the aerospace industry often involve the machining of large titanium forgings. The forging process is usually done by an external contractor and tends to involve long lead times. In addition, forging is usually inefficient in terms of the energy and material consumption. In contrast, LMD is a powerful tool that could be used to overcome these difficulties. Due to the small dimensions of commercial LMD machines, they can be easily installed in workplaces, thereby reducing the lead times as well as the number of subcontracted tasks. The buy-to-fly ratio of titanium aerospace components manufactured by conventional subtractive manufacturing techniques may be as high as 20:1 [56], rendering these processes inefficient and reducing the sustainability of the part life cycle. On the contrary, LMD can achieve buy-to-fly ratios in the range of 1.5–5:1 [56]. The design freedom

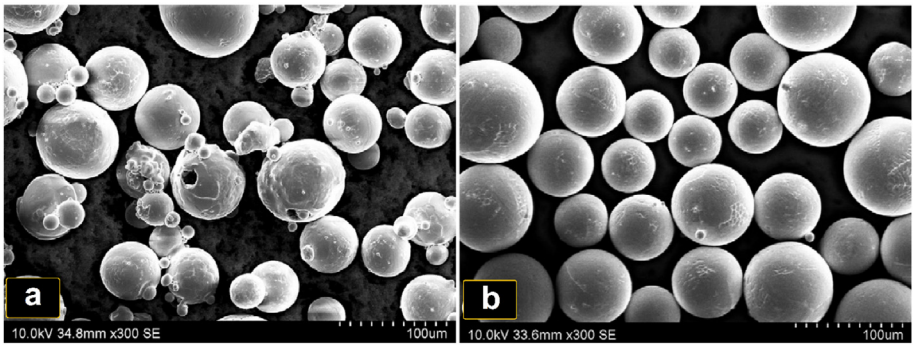

Fig. 4. The SEM images of the Ti–6Al–4V powders produced by (a) GA and (b) PREP for LMD applications [49].

offered by LMD can be also used to fabricate topologically optimized parts that tend to be geometrically very complex but weigh less. Furthermore, complex design features that ordinarily require long machining times can be fabricated faster using LMD. Finally, LMD does not require the fabrication of expensive tooling every time a new part needs to be built, further increasing the associated cost savings.

As for the disadvantages, LMD consumes high amounts of energy given its use of a high-power laser beam. This may, however, more than be compensated for by the energy saved as a result of shorter manufacturing times and reduced post-treatment steps. Additionally, the poor surface finish and geometrical inaccuracies inherent to such a lay-by-layer process (*e.g.*, the staircase effect) are the common drawbacks of the LMD technology. Although using a smaller layer thickness minimizes the staircase effect, the production time will increase. Moreover, geometrical inaccuracies and a poor surface finish may necessitate post-processing steps that increase the production time and cost.

As opposed to SLM, where the powder bed acts as a support for the fabrication of overhanging structures, LMD has no natural support mechanism. Even though the production rate of LMD is much higher than other AM techniques such as SLM [57], limited productivity (as compared to some other conventional manufacturing process) remains a major challenge that needs to be overcome through additional developments. To put this limitation in perspective, deposition rates of up to 0.45 kg/h have been reported using wire feedstocks [58], while values of up to 0.9 kg/h have been achieved with powder-blown LMD processes [14]. The high initial cost of the required equipment and expensive feedstocks have been the other deterrents for the potential users of the LMD technology.

When comparing powder-based and wire-based LMD, the former suffers from a high surface-to-weight ratio and an increased possibility of atmospheric contamination. A high deposition efficiency, favorable deposition rate, good availability, and simpler feedstock handling and storage are the other advantages of wire-based LMD. Especially for Ti–6Al–4V, the contaminants might strongly affect the mechanical properties of the resulting parts [50]. In addition, powder is two to three times more expensive than wire [59]. Despite these advantages, less attention has been paid to wire-based manufacturing of Ti–6Al–4V components [50].

Many materials have been successfully processed using LMD including titanium alloys [50], stainless steels [60], tool steels [61], nickel-based alloys [57], cobalt-chrome alloys [62], and aluminum alloys [63]. Materials with a high reflectivity and considerable thermal conductivity are usually difficult to process by laser-based AM processes such as LMD. Powder materials generally have absorptivity values that are twice as much as that of the same materials with flat surfaces. That is because metallic powders scatter and entrap the laser light [64]. Given that the absorptivity of powder material is, nevertheless, low, a high portion of the incident laser beam is reflected. A high laser power is therefore needed to generate a melt pool. Similarly, materials with high thermal conductivity can rapidly transfer the laser beam-generated heat to the bulk material, thereby reducing the temperature and effectiveness of the melt pool [64].

4.2. Physical phenomena

In LMD, the previously deposited layers may partially re-melt when the subsequent layers are deposited [50,65]. This can lead to a banded microstructure. To prevent this from happening, some studies have suggested that the process should be stopped in between the layers to make sure the temperature of the previous layers stays below a certain threshold [50,65]. For instance, Nassar et al. [66] have proposed an intralayer closed-loop real-time control system that ensures the temperature of the previous layer stays below 415 °C.

In general, a fine or equiaxed microstructure increases the strength and ductility of the material while a coarse or lamellar microstructure has the opposite effects. Higher laser powers usually lead to coarser columnar grains as well as thicker layers and bigger heat affected zones. (HAZs). Fig. 5 shows the microstructure of the formed melt pool and its neighboring heat affected zone for

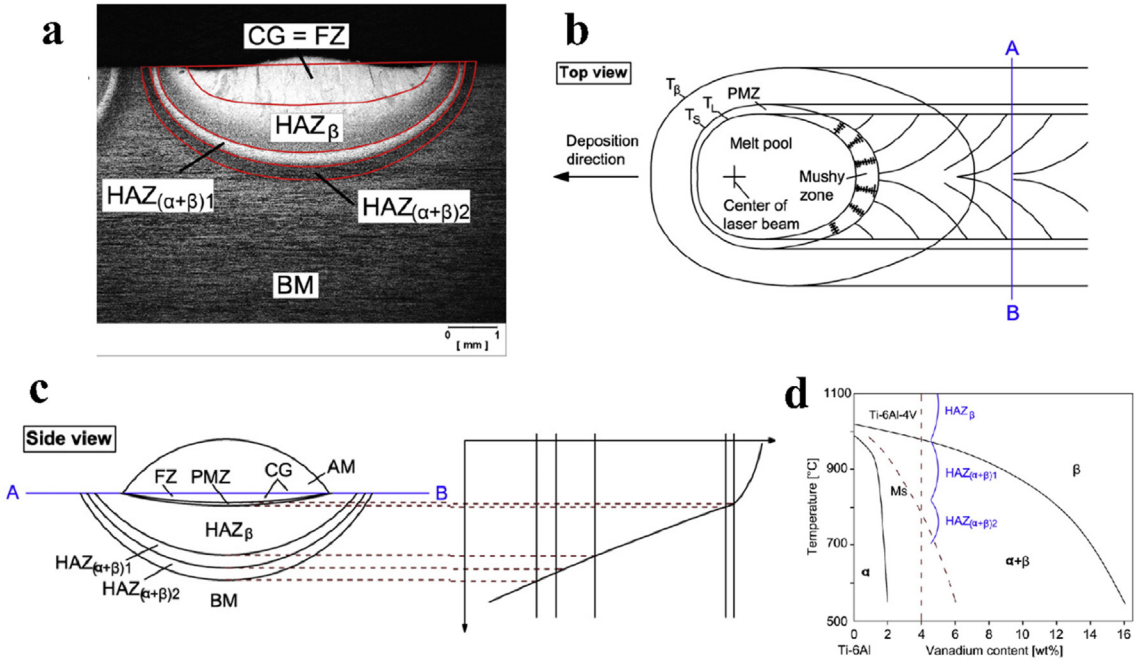

Fig. 5. (A) A cross-sectional image of LMD Ti–6Al–4V parts showing various HAZs; (b) A top view of the melt pool and heat affected zone; (c) A side view of the melt pool, the heat affected zone, and the thermal gradients present in different depths; and (d) A binary phase diagram of (Ti–6Al)–V alloys indicating the temperature zones corresponding to the different types of the heat affected zone [67].

LMD Ti–6Al–4V. The region below the dilution area typically consists of several zones [52,67]:

(i) **The based metal (BM) zone**, which is not affected by the generated heat and its microstructure is the same as the as-received base material (*e.g.,* globular primary α grains in a basket-weave (α+β) matrix);
(ii) **Binary (α + β) heat affected zone ($HAZ_{\alpha+\beta}$)** whose local temperature is sufficiently high but below T_β, meaning that its microstructure will contain a combination of α and β phases. This region can be classified into two distinct zones depending on the local thermal gradient and the cooling rate, namely $HAZ_{(\alpha+\beta)1}$ and $HAZ_{(\alpha+\beta)2}$. In the region $HAZ_{(\alpha+\beta)2}$, the peak temperature is not sufficiently high to change the microstructure of the base metal except for the facts that the lamella width of the basket-weave (α+β) matrix may slightly increase while the average size of the primary α grains remains constant. In the region $HAZ_{(\alpha+\beta)1}$, however, the peak temperature is higher than the BM and $HAZ_{(\alpha+\beta)2}$ zones, but below T_β. Therefore, the basket-weave (α+β) binary structure of the matrix tends to transform into a colony structure with finer α lamella.
(iii) **HAZ_β zone** whose peak temperature is higher than T_β, resulting in substantial change in the microstructure oberved in this zone. Depending on the applied peak temperature, the primary α grains are either refined or are completely dissolved in the HAZ_β zone, whereas the prior β grains begin to slightly coarsen.

4.3. Processing parameters

LMD parts are affected by a variety of processing parameters and their combined interactions. The optimization of these parameters and, thus, the resulting microstructures and mechanical properties is of critical importance not only because it enables LMD to be competitive against conventional manufacturing techniques but also because it qualifies this process for the fabrication of functional parts. The control and monitoring of these parameters through closed-loop feedback control and live data acquisition systems is of great potential utility in this regard.

The incident energy applied during the laser-material interaction process is a commonly used parameter when evaluating the effects of a processing parameter on the properties of the finished part. The energy density calculated using the laser processing parameters allows for the evaluation of the range of the parameters by which metallic parts can be fabricated with satisfactory properties [31] and is calculated as:

$$\textit{Energy Density} = \frac{\textit{Laser Power}}{\textit{Laser Scanning Speed} \times \textit{Laser Spot Diameter}} \left(\frac{J}{mm^2}\right) \quad (1)$$

It is important to realize that even though the energy density is the most commonly used parameter in the literature of AM processes, it is not necessarily the best parameter for describing the complex physics of the melt pool.

LMD may be operating either under the conduction or the keyhole regimen. Under the latter mode, the power density of the laser beam is so high that a plasma phase forms and the metallic material evaporates [68]. The evaporation of the feedstock results in the development of a vapor cavity that enhances laser absorption, enabling the laser beam to "drill" much further into the material than it is possible in the conduction mode [68]. The deep pores formed in the keyhole model result in the lower densities of the finished part [69]. It is therefore desirable to make sure LMD always operates under the conduction mode. However, the energy density per volume of processed material is not an appropriate metric to quantify the melt pool depth and to detect the transition between the conduction and keyhole modes [69].

To optimize the processing parameters, usually the laser power and traverse velocity are modified while the laser spot diameter is kept constant within the range of 1–3 mm [31]. The traverse speed often ranges between 1 and 20 mm/s, while the laser power is in most cases kept at levels between 1 and 4 kW [31]. As inferred from Eq. (1), a combination of a higher traverse speed and a lower laser power results in a lower incident energy. This combination gives rise to finer microstructures due to higher cooling rates. On the contrary, coarser microstructures can be achieved with lower cooling rates resulting from a decreased traverse speed and an increased laser power [31].

In LMD, the laser beam is focused on one specific point, where the powder should be blown. Therefore, the stand-off or focal length of the LMD nozzle with respect to the substrate affects the performance of the process. The variations in substrate position induced by misalignment, overbuilding, or in-process distortion will bring about variations in the powder feed alignment or energy density [70]. The thermal monitoring of the melt pool can be implemented by using infrared cameras and/or pyrometers. The temperature data obtained using the thermal monitoring systems can then be used for on-the-fly adjustment of the processing parameters or for quality assurance purposes [31].

The type of the laser scanning pattern is another process-related variable that could be used to tailor the microstructure and mechanical properties of the resulting material. For example, Nickel et al. [71] studied the effects of the raster, offset-out, and fractal deposition strategies on the geometrical accuracy of the LMD parts. They found that the fractal and offset-out patterns generate the smallest possible levels of the substrate deformation.

As another determining factor in LMD, the powder flow rate affects the intralayer porosity. In a case study, an optimum powder flow rate of 0.033 g/s was reported to give the lowest intralayer porosity level both for GA and PREP powders regardless of the applied laser power (*i.e.*, 800 or 1000 W) [49].

A limited number of studies have addressed the ways through which different combinations of processing parameters influence the microstructure of the final part. In particular, the laser scanning and deposition strategies play important roles in the microstructure and properties of the resulting material. For example, Dinda et al. [72] have shown that alternating the layer-to-layer scanning direction in LMD of Inconel 625 rotates the growth direction of the columnar dendrites by 90°. Kobryn et al. [73] addressed how the variation of the laser power and transverse speed can influence the width of the prior β-grains. They observed that the grain width decreases with the traverse speed but remains unaffected by the laser power (Fig. 6), which is expected given that the grain size tends to decrease with the cooling rate. High cooling rates arise from a combination of a low laser power and a high traverse speed, leading to smaller grain sizes [74].

In addition to the processing parameters, the properties of the (powder) feedstock can radically change the properties of the final LMD components. For instance, the Ti–6Al–4V powder made by PREP results in a higher layer thickness as compared to GA powder for all values of the powder flow rate and laser power [49].

4.4. Microstructure evolution

The microstructural features of LMD parts strongly depend on their thermal history during the fabrication process. This includes

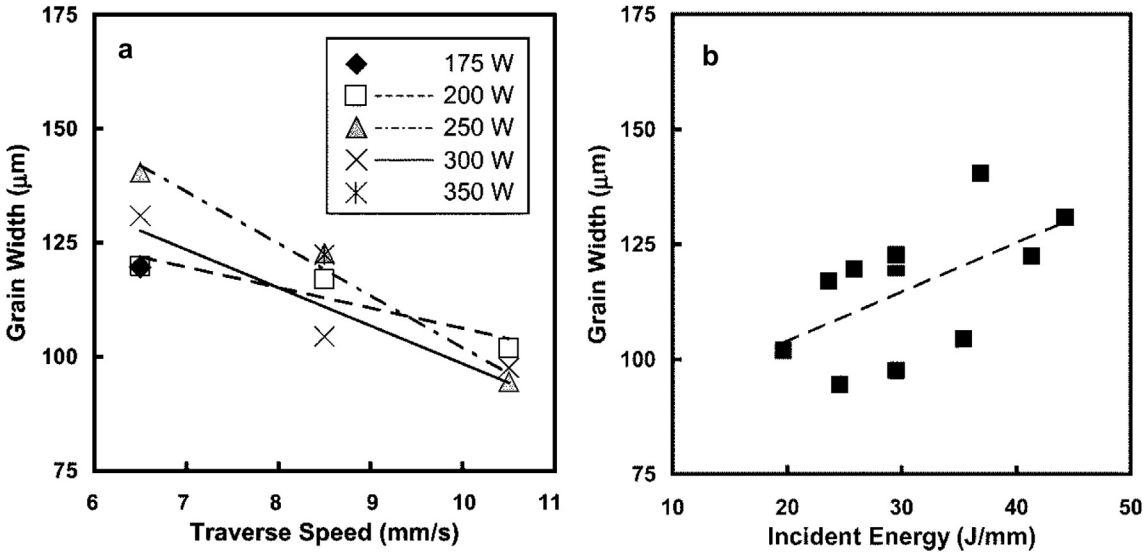

Fig. 6. The variation in the grain width as a function of (a) the traverse speed and (b) incident energy [74].

high cooling rates, significant temperature gradients, and the increase of the temperature of the bulk material. Since many processing parameters interact in complex ways with each other to determine the thermal history of LMD parts and to define the solidification process, the precise prediction of the evolved microstructure is still a major challenge. Depending on the cooling rate, equiaxed grains, elongated columnar grains, or a combination of both may form [75]. It has been found that a higher solidification rate promotes the transition of the columnar grains to equiaxed grains whereas a higher cooling rate leads to a finer microstructure [75]. The cooling rate is affected by other processing parameters such as the laser power and scanning speed too. LMD Ti–6Al–4V is highly sensitive to the formation of columnar grains in a broad range of laser powers and scanning speeds. The columnar grains start coarsening when the laser scanning speed is reduced or the laser power is increased [75]. In particualr, the microstructure of LMD Ti–6Al–4V parts shows directional columnar β grains that are in parallel with the deposition direction and very fine α-phases with different morphologies that are dependent on the applied laser power [76,77]. With a low laser power, the α morphology exhibits acicular α′ microstructures while application of higher laser powers or post-heat treatments give rise to fine α+β lamellae with α' martensitic microstructures [78].

The grains formed during the LMD process are generally smaller near the interface with the substrate as compared to the subsequent layers [79]. The lack-of-fusion pores and cracks are some of the commonly observed defects in these products. Pores are reported as the preferential sites for the initiation and propagation of cracks [79]. The presence of pores at the interface between two subsequent layers is referred to as "interlayer porosity" or "lack-of-fusion" porosity [80–82]. The interlayer porosity usually appears at the boundary of different layers due to insufficient energy input in the process [83]. The interlayer porosity can be controlled to some extent by adjusting the processing parameters, but there is still disagreement over the main source of intralayer porosities and whether the process conditions, process parameters, or initial powdery materials are the dominant causal factors [83]. The pores generated by the entrapped gas are also a common feature in LMD parts and are known as the "intralayer porosity". These pores are generated by the gas captured from the surrounding atmosphere or are formed within the melt pool [84]. In fact, the melt pool is subjected to intense convection due to the Marangoni-induced flows [84]. The flowing metal of the melt pool may carry the gas from the atmosphere, thereby leading to gas entrapment in the melt pool [84]. This phenomenon occurs specially when the solidification time is too short for the gas bubbles to escape to the surface [84]. The Marangoni convection refers to the tendency of heat and mass to travel to the areas within a liquid that have higher surface tensions. It usually occurs under high surface tension gradients. Since the Marangoni flows are accelerated when the laser power increases, a higher laser power enhances the possibility of entrapping the gas between the powder particles [49].

The cracks caused by residual stresses are often observed in LMD parts. These stresses arise from the dynamic temperature distribution and high heating and cooling rates experienced during the LMD process. The presence of residual stresses may lead to a reduced strength, a reduced service life, and increased dimensional inaccuracies due to the warping effects [31].

5. LMD of Ti–6Al–4V

The evolved microstructure of LMD Ti–6Al–4V parts highly depends on the cooling rate experienced during the deposition process. The cooling rate is determined by the geometry of the part, the processing parameters (*e.g.,* laser power and laser scanning speed), and the properties of the involved materials (*e.g.*, thermal conductivity of the substrate and the deposited layers) [75–77,85,86]. Columnar prior β grains have been found to grow along the build direction in LMD Ti–6Al–4V [87]. A disruption in this growth regimen produces a more equiaxed, fine, and randomly orientated grain structure [87]. Indeed, the application of a light deformation step after every layer has been found to promote the refinement of β grains, thereby improving the mechanical properties and isotropy of the resulting material [87].

In the early stages of an LMD process, when the substrate is still cold, the deposited layer cools down very quickly through heat dissipation by conduction to the substrate and a martensitic structure is formed. The cooling rate decreases as the substrate heats up, resulting in the formation of the Widmanstätten structure [80,88–90]. In recent years, the effects of the cooling rate on the formation of the different microstructural phases have been studied. In this case, the cooling rate has been changed by varying the

processing conditions [89,91,92]. The full α' martensitic microstructure has been found to form at cooling rates above 410 °C/s while a mixed $\alpha' + \alpha_m$ (secondary α morphology) structure is evolved for the cooling rates ranging between 20 and 410 °C/s. Cooling rates below 20 °C/s often result in the Widmanstätten-type of microstructure [89].

The microstructure of LMD Ti–6Al–4V parts is characterized by defects such as the lack-of-fusion porosities, cracks, voids, and the defects resulting from droplet spattering [93]. Residual stresses can also be developed during the process [94]. Due to the high temperatures required for melting metallic materials and the high cooling rates generated in the LMD process, high thermal gradients are induced around the melt pool, provoking thermally induced residual stresses [95,96]. As the molten material solidifies, the temperature of the upper layer increases to values higher than that of the previously solidified ones. As the upper layer cools down and shrinks, plastic deformations begin to develop, because the thermal strains exceed the yield stress of the material, and are mainly controlled by the magnitude of the thermal gradients in the solidified metal [86,97]. These residual stresses can decrease the fatigue resistance of the LMD part, as they provide an additional driving force for the initiation and propagation of cracks [95]. Moreover, they give rise to geometrical inaccuracies [98,99]. As a standard practice, a trial-and-error approach is employed to minimize the residual stresses and distortions in AM. This approach is costly and time-consuming. Alternatively, computational models such as those based on the finite element method (FEM) could be used to predict the thermomechanical behavior of LMD Ti–6Al–4V and to optimize the processing parameters [100]. Such computational models can precisely predict the mechanical behavior of the material, but require long computational times and skilled users.

Voids and lack-of-fusion pores are commonly observed on the fracture surface of LMD Ti–6Al–4V parts [101]. These defects can substantially degrade the mechanical properties of the material. The initial voids are usually cycloidal or elliptical with diameters in the range of 1–10 μm and a very smooth inwall [30]. The voids are created when there are impurities in the powder particles or when the gas present in the hollow space between the particles does not have sufficient time to escape during the solidification process [30] (Fig. 7). Paydas et al. [52] have reported randomly distributed gas pores with a globular shape and an average diameter of 20 μm. However, Amsterdam et al. [79] reported much bigger pores of up to 86 μm in diameter.

Too low temperatures in the melt pool or excessively high powder feed rates may cause inadequate melting of the powder particles [30]. As a result, the previous layer does not fully re-melt as the subsequent is deposited, leading to the formation of the lack-of-fusion defects at the interface between both layers [30]. The lack-of-fusion defects have irregular shapes and sizes and can give rise to anisotropic mechanical properties of the LMD material [30]. Biswas et al. [102] have investigated the effects of porosity on the plastic deformation and fracture behavior of LMD porous Ti–6Al–4V parts under both static and dynamic loading conditions. They found that LMD Ti–6Al–4V alloy with 20% porosity exhibits lower levels of strength but higher ductility as compared to the same type of material with a porosity content of 10%. Similarly, LMD Ti–6Al–4V with 10% porosity exhibits a lower strength but higher levels of ductility than a fully dense material of the same type [102]. It has been suggested that the formation of adiabatic shear bands is the main failure mechanism of these LMD materials [102].

5.1. Finite element analysis

As previously stated, predicting the potential effects of the processing parameters on the melt pool behavior is of crucial importance for the optimization of the microstructure and the mechanical properties of LMD materials. FEM models are often used for this purpose as well as for a quantitative analysis of the residual stresses resulting from the LMD process. Finite element analysis (FEA) of the LMD process is inspired by the models of the welding processes, because welding is a similar process that has been extensively studied for decades using a variety of computional models. The computational models developed for welding processes usually neglect convection or the applied free convection. These assumptions are valid when the amount of the deposited material is small as compared to the size of the substrate. Given their much higher amount of the deposited material, the level of convection is much higher in LMD processes as compared to the welding processes, rendering the existing models inaccurate [103]. Temperature, residual stress, and *in-situ* distortion measurements are usually carried out in these studies [53,104]. Despite the dynamic nature of the LMD process, the simulations performed thus far have been mostly quasi-static in nature. Sequentially coupled thermal and mechanical FEA is widely used [53,104] in order to save computational cost. A thermal FEA is generally performed first followed by a mechanical FEA performed using the thermal loads obtained in the first analysis step. Another commonly used technique is the *ad hoc* activation of otherwise quite elements [100]. When the elements of a layer are first introduced, they are “quiet”, meaning that their mechanical properties are so small that they do not affect the analysis before they are activated. This approach has been used in the studies carried out by Heigel and Yang [103,104].

Coupled thermomechanical models with an ellipsoidal laser beam representation have been used by Lundbäck et al. [53]. In that study, the in-plane geometry of the beam was elliptic but the size of the ellipse linearly decreased with depth. Similarly, the in-plane distribution of the beam shape was Gaussian but linearly decreased through the depth. This technique allowed for a good

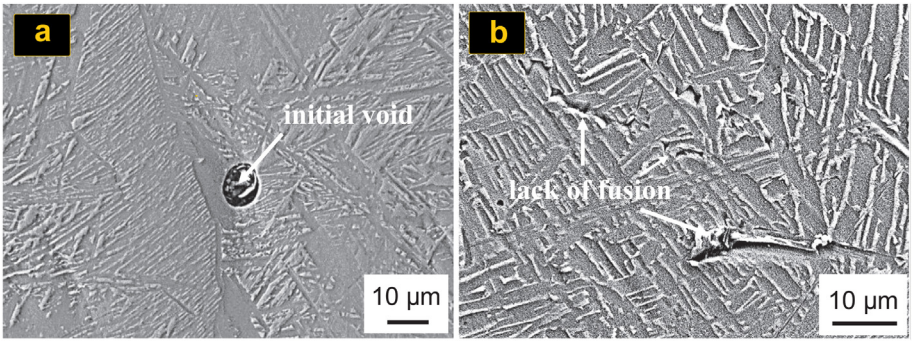

Fig. 7. The SEM images of the Ti–6Al–4V parts produced by LMD showing the presence of initial voids and the lack-of-fusion pores [30].

representation of the high-power energy sources similar to the ones used in LMD. The largest residual stresses were observed along the build direction, with stresses along y and z axes close to zero [53]. For modeling the input heat, the simplest approach is to assume that the temperature of the newly deposited material equals its melting temperature [105,106]. More complex heat source models involve employing a volumetric heat flux and the assumption that the powder particles reach the melting temperature during the flight across the laser beam. The heat loss to the surroundings is commonly modeled as convective and radiative [103,104]. Yang et al. [104,107] have employed an elastic and perfectly plastic material models, ignoring the potential kinematic hardening phenomena. This was motivated by the limited work hardening they observed for Ti–6Al–4V that was plastically deformed under the tensile forces resulting from XXXXX. Heigel et al. [103] and Yang et al. [104] have proposed the element distribution of 1 element high and 2 elements wide per clad. They also used temperature-dependent mechanical properties such as the Young's modulus, yield strength, and thermal expansion coefficient. Most of the FEM models have found a good agreement between the experimental and computional value of stresses for both mechanical and thermal analyses [ ]. However, a study carried out by Heigel et al. [103] demonstrated that the implementation of a measurement-based forced convection model is necessary for an accurate FEA of the LMD process. This study showed that the measurement-based forced convection model could achieve temperature errors of less than 11%, while errors of up to 44% are encountered when a free convection model is applied (Fig. 8). As for the residual stresses, both free convection model and forced convection model predicted similar values of the residual stresses that were close to the measured ones (Fig. 8). In a study by Yang et al. [104], an ellipsoidal volumetric heal flux model with an absorption efficiency, η, of 45% was used. They also assumed the intersection between the heat source ellipsoid and the top surface of each deposition track to be circular while using a penetration depth to width ratio of 0.45. The density was assumed to be constant, and an average forced convection coefficient of $h = 55$ was employed.

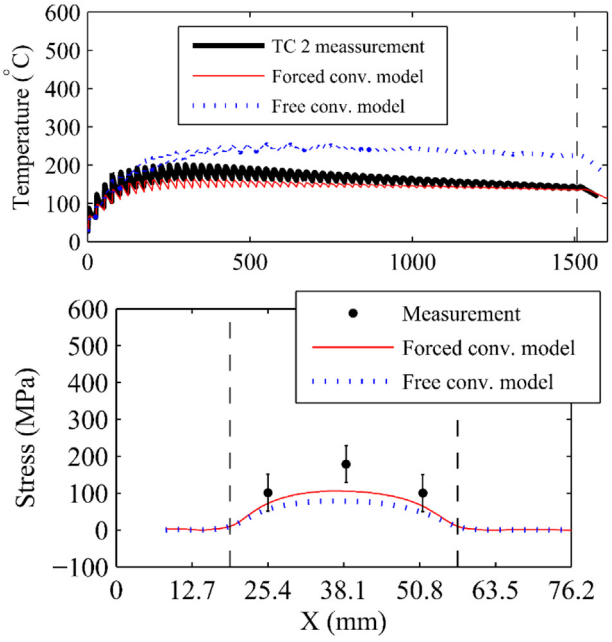

Fig. 8. (A) The temperature history for the forced and free convection models as compared to thermocouple measurements and, (b) a comparison of the predicted and measured residual stresses [103].

5.2. Microstructural evolutions

The microstructure of LMD Ti–6Al–4V consists of different phases present in a β matrix. The prior β grains grow epitaxially crossing multiple layers with a slight inclination with respect to the build direction [108]. In a case study, the average width of these grains has been reported to be around 0.5 mm [109]. Unlike these systems, the typical microstructure of wrought Ti–6Al–4V parts lacks columnar grains and consists predominantly of equiaxed grains. The types of the microstructures present within the β grains include the primary α, secondary α, plate-like α, colony α, hcp martensite (=α′), grain boundary α, acicular α, Widmanstätten, and basket-weave. The "Secondary α" forms upon heating and cooling in the α+β region within a temperature range of 815–900 °C [110,111]. The commonly used etchant for Ti–6Al–4V is 18% HCl (hydrochloric acid) + 11% HF (hydrofluoric acid) in water [112]. Other researchers have used the Kroll's etching reagent with 2% HF (hydrofluoric acid) + 6% HNO_3 (nitric acid) and 92% deionised water [30].

The crystallographic microstructures within the β grains consists of a series of needle-like martensitic α phases, a large number of Widmanstätten α-laths structures, and a few β phases between the α-laths [113]. Donoghue et al. [87] have also shown the presence of twinned α at the β grain boundaries. These twinnings are usually formed on the α lath boundaries and originate from a tensile $\{10\bar{1}2\}$ twin, which is commonly observed in titanium and has been previously observed in deformed Ti–6Al–4V [114]. As illustrated in Fig. 2, needle-like martensitic α-phase clusters are arranged in parallel to and regularly along the β grain boundaries [30]. Within the β grains, the Widmanstätten α-laths structures are woven into the basket-weave microstructures [30]. Both the needle-like martensitic α-phase clusters and Widmanstätten α-laths present thin and needle-shaped microstructures, which exhibit high levels of strength. However, the coarser Widmanstätten α-laths have been also found along the β grain boundaries (Fig. 2) [30]. These coarser Widmanstätten α grains are thicker, with lengths <10 μm, and are caused by the deformation applied to the tested specimens. The coarse Widmanstätten α-laths reduce the strength of the material through weakened inhibition of the dislocation glide. Indeed, when a large amount of the α-lamellae phases precipitate along the β grain boundaries, the dislocations glide smoothly and the yield strength of the material decreases [30,58,115].

The grid structures, akin to those shown in Fig. 9b, are observed by many researchers as an evidence of the formation of a martensitic phase [116–118]. Some studies argue that the cooling rates are so high in LMD that the martensitic transformation is to be expected [50,111,119]. In general, slow cooling rates lead to the formation of colony structures, while intermediate cooling rates result in basket weave structures, and fast cooling rates elicit the martensitic transformations. The diversity of the microstructures observed suggests that the microstructural evolutions during LMD is controlled by the final cooling rate from the β-transus to the extent that the thermal cycles below the β-transus temperature may have a minimal effect [50,111,119]. The common cooling rate in LMD is around 3500 °C/min (= 58.3 K/s), which is above the cooling rate at which the Widmanstätten structure is transformed into a martensitic α' (*i.e.*, 1000 °C/min = 16.7 K/s) [26,110,119]. The martensitic α' structure can be transformed into a fine lamellar α+β microstructure by annealing treatments within the temperature range of 700–850 °C.

The high mechanical strength of Ti–6Al–4V (*i.e.*, a α+β alloy) originates from the synergistic effects of multiple important phenomena. The main strengthening mechanisms include solid solution strengthening from the substitutional (*e.g.*, vanadium and

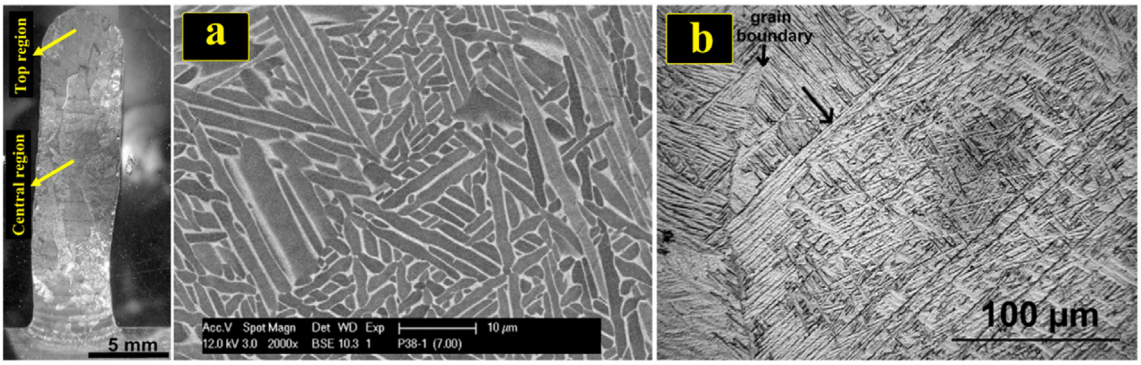

Fig. 9. The microstructure of LMD Ti–6Al–4V in the central (a) and top (b) regions [50].

aluminium) and interstitial elements (*e.g.,* oxygen, nitrogen, and carbon) as well as boundary strengthening from the grain boundaries, phase boundaries, and lamella boundaries present within the microstructure [55,110]. While oxygen is known to enhance the interstitial strengthening, it can lower the ductility at higher levels. The precipitation hardening of the α-phase occurs by coherent $Ti_3Al(\alpha_2)$ particles [55,110]. Upon annealing in the α+β-region, a significant partitioning of the alloying elements may take place and the α-phase is enriched in the α-stabilizing elements (Al, O, Sn) [55,110]. A substantial volume fraction of coherent Ti_3Al particles can then be precipitated in the α-phase by aging, for example, at 500 °C [55,110].

If one cuts LMD specimens along their build direction, layered bulges parallel to the deposition plane, as well as large elongated columnar grains can be observed. These elongated grains are the prior β grains, which have epitaxially grown across the welding layers [111]. When a new layer is deposited, the surface of the previous one is remelted, and the epitaxial growth of the prior β grains occurs from the previous layers [111]. In a case study, the prior β grains were inclined 30° relative to the z-direction, a result of the laser beam traveling along the direction of heat dissipation [74]. This fact has been also reported by Sridharan et al. [111] where they observed a significant change in the crystallographic texture from {90°,90°,0°} in the first layer to{90°,30°,0°} after the deposition of the fourth layer. Similarly, other authors have reported a prior β grain orientation of 45° with respect to the build direction [58]. An analysis of the crystallographic orientation of residual β grains contained between the α-laths has demonstrated very little change in the orientation both at the room temperature and at 800 °C [87]. At 850 °C, the β phase starts to grow from the fine residual β grains, following the preferred orientation of the residual β grains [87]. At temperatures slightly below the β-transus temperature, the phase transformation progresses to the point where the β phase covers approximately 35% of the specimen [87]. At this temperature, a new orientation of the β grains is observed, which is located within the region of the α-twins (Fig. 10) [87].

A stress-relief treatment is generally recommended for aerospace components after the LMD process [120]. The appropriate

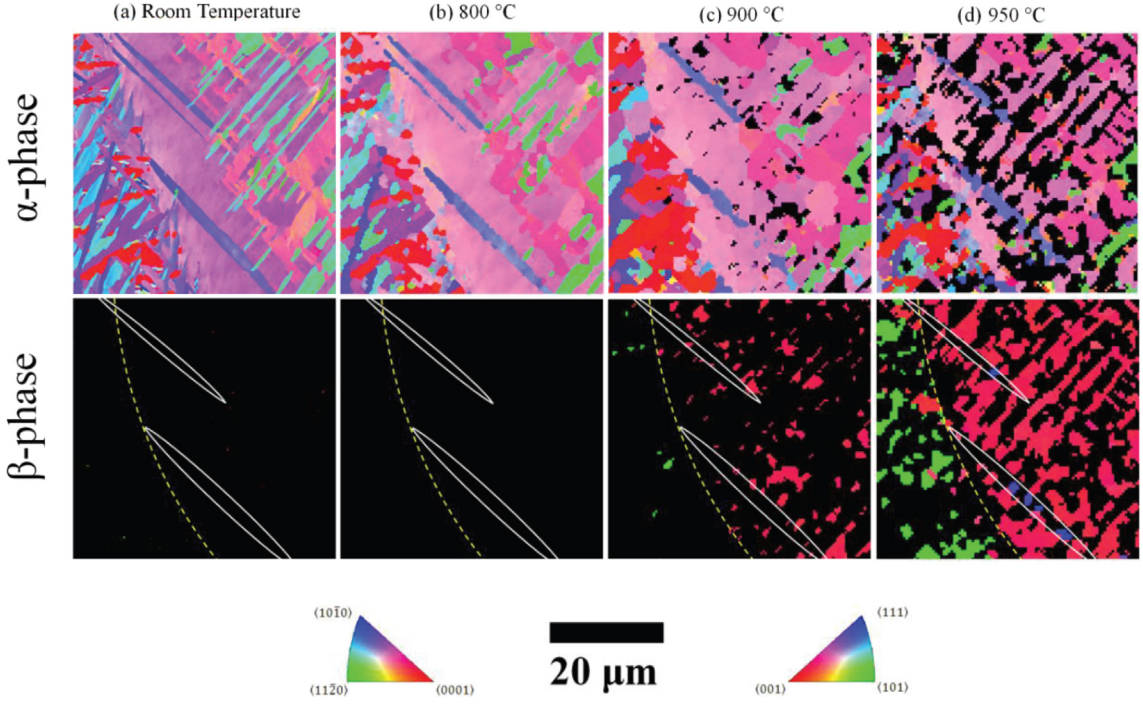

Fig. 10. The EBSD maps of LMD Ti–6Al–4V parts showing grain growth and grain orientation as a function of the temperature [87].

temperatures for this treatment may vary, but the temperatures of 600 °C [50] and 704 °C [42,65] have been reported in the literature. The post-AM heat treatment of Ti–6Al–4V parts is typically performed according to the SAE standards at the α+β-region temperatures (<T_β = 995 °C). Although these treatments do not remove the primary defects generated in the process, they are capable of altering the distribution, size, and morphology of the α-phase being formed upon cooling from above the β-transus temperature [109]. However, these treatments do not show a signficant impact on the prior β grains. A variety of morphologies have been reported for the α grains after subtransus heat treatments. The α-dissolution temperature has been reported to be 708 °C, 677 °C, or 747 °C [110,121]. Since heat treatments at temperatures considerably higher than T_β lead to a complete dissolution of the α phase, they are not typically applied due to the challenges associated with grain coarsening, high energy consumption, material handling, and the embrittlement of the layers close to the surface. Brandl et al. [112] have evaluated the potential effects of various heat treatments on the hardness and microstructure of LMD Ti–6Al–4V parts. They showed that the hardness of the parts is not affected by the time spent at the temperatures above T_β, and that the transformation of the columnar to globular prior β grains is feasible by heat treatments above T_β. Additionally, they reported a homogeneous basket-weave structure after application of a solution treatment at a temperature above T_β, quenching, and annealing. They concluded that heat treatment at 600 °C for 4 h followed by furnace cooling could considerably increase the hardness of LMD parts, while the same thermal procedure at 1200 °C for 2 h greatly decreases the average hardness of the specimens [110,112].

6. Mechanical properties

The relationship between the microstructural features and mechanical properties of LMD parts is not yet fully understood. It is, however, known that LMD Ti–6Al–4V exhibits high levels of anisotropy with respect to the build orientation [122]. Moreover, several studies have found that as-deposited LMD Ti–6Al–4V can achieve strength and ductility values close to those of wrought Ti–6Al–4V (AMS 4928) [50,55,123]. Due to the anisotropic nature of HCP crystals, the mechanical properties of Ti–6Al–4V are strongly dependent on the α texture developed during LMD. Ti–6Al–4V deforms through a twinning plastic deformation mechanism [124,125]. Under tensile forces, the majority of titanium alloys show the presence of tensile twin deformation systems $\{10\bar{1}2\}$. Donoghue et al. [87] have confirmed the presence of the twinned α inside a band of colony α. Table 4 presents a summary of the main microstructural features and mechanical properties reported for LMD Ti–6Al–4V in the literature.

The LMD process is characterized by the heterogeneous nucleation as well as directional and rapid solidification of the deposited material. Therefore, the morphology and microstructure of LMD Ti–6Al–4V can be compared to those obtained by casting (ASTM F1108). Given its fast solidification process, the microstructure of LMD parts is usually finer than that of those cast, leading to higher strength values [65]. However, the ductility of LMD Ti–6Al–4V is usually below those reported for as-cast Ti–6Al–4V [65]. Elongation values as high as 9% have been reported, which is half of the values found for the Ti–6Al–4V commercial duplex alloy [50,52,55]. This low ductility can be attributed to the remaining residual stress in the specimens, martensitic decomposition [1], and defects orientation [2]. Heat treatments at 600 °C do not change the elongation at failure, while those at 843 °C increase it [29,126,127]. The thermal decomposition of the martensitic α′ phase into a α+β lamellar structure at 730 °C can explain this observation, as a lower amount of the hard α' phase increases the ductility and decreases the strength of the material [29,126,127]. Moreover, the ductility of laser-processed AM-fabricated Ti–6Al–4V depends on the orientation at which the parts are printed, because the spatial orientation of defects varies with the printing direction [127]. It has been shown that the ductility along a direction perpendicular to the build plate is lower than that along the horizontal direction [127]. The tensile strength and hardness are not significantly influenced by any of these heat treatments [50,55]. In a study conducted by Carroll et al. [122], the beneficial effects of an additional 0.0125 wt% oxygen on the tensile and yield strengths of Ti–6Al–4V was confirmed, as well as a slight decrease in ductility.

Hot isostatic pressing (HIP) is another post-treatment process that can be implemented to improve the microstructural features and geometrical fidelity and enhance the quasi-static and fatigue properties of LMD Ti–6Al–4V parts. During the HIP process, the materials are simultaneously subjected to elevated temperatures and high pressures for an extended period of time. The process is performed isostatically in a high-pressure vessel that is usually equipped with an inert pressurizing gas (*e.g.,* argon) so as to prevent chemical reactions [128]. An example of a standard HIP process for LMD Ti–6Al–4V parts (*i.e.*, temperature = 920 °C, pressure = 100 MPa, duration = 4 h) followed by furnace cooling (with a cooling rate of around 5 °C/min) has been recently proposed [129]. The process can help eliminate the defects formed during LMD including the micro-porosities created as a result of gas entrapment [129]. Closing these micro-porosities can also increase the density of these components. HIP may also be used to remove the distortions induced during the LMD process, thereby improving the geometrical fidelity of the treated parts. Furthermore, the heat treatments involved in the HIP process could cause a phase transformation from martensite to $\alpha + \beta$ phases. Such a phase transformation can improve the ductility of LMD Ti–6Al–4V parts while somewhat decreasing their yield and tensile strengths [129] and mitigating their mechanical anisotropy [31,73,129]. Closing the internal defects that originate from the LMD process could also significantly enhance the fatigue life of LMD Ti–6Al–4V components [31,130].

6.1. Tensile and compressive properties

The tensile and compressive strengths are the most commonly studied properties of LMD Ti–6Al–4V. In general, the ultimate tensile strength (UTS) seems to be directly affected by the applied heat treatments [50]. Moreover, the elongation corresponding to the UTS of LMD Ti–6Al–4V has been found to increases through heat treatments at 843 °C for 2 h [50].

The tensile tests are usually performed at the room temperature following the EN10002 standard, and the results are often compared to the lower band of the wrought Ti–6Al–4V properties (ASTM B348) and their plastic deformation behavior at elevated temperatures [60]. There is a widely held consensus among researchers that during the plastic deformation of LMD Ti–6Al–4V, no more than 10% of the plastic work can be stored in the material as the internal energy [109]. The rest of the applied energy is either dissipated in the case of quasi-static loading or increases the overall temperature of the deformed material [109]. In quasi-static loading, the plastic deformation-induced heat flow has enough time to diffuse inside the material. On the contrary, at high strain rates, the rate of heat generation is higher than that of dissipation. In this case, the heat does not have enough time to be dissipated and, consequently, the temperature of the specimen increases [109]. Therefore, dynamic stress-strain curves are adiabatic lines on which the corresponding temperature increases with the applied strain level. An increment in the temperature usually leads to a

Table 4
The processing window for LMD of Ti–6Al–4V components and the resulting microstructural features and mechanical properties.

Machine type	Laser type and power	Characteristics of starting powders	Substrate	Microstructural features	Defects	Significant conclusions	Mechanical properties	Ref.
6 axis Kuka KR16 robot and 2 axis table	Trumpf HLD 3504 Nd:YAG diode laser. Maximum power: 3.5 kW	Wire (1.2 mm in diameter)	Ti–6Al–4V			The stress-relief heat treatment at 600 °C does not have significant influence on the mechanical properties. However, the heat treatment at 843 °C increases the strain at failure.	- Fatigue limit: 750–913 MPa - Vickers hardness: 326–392 HV - UTS: 900–1000 MPa	[50]
	Photonics YLR-12000 coupled with a Precitec YW-50 laser optic Used power: 2 kW	PREP-produced powder supplied by TIMET Powder Metals, LLC. D10 of 58 μm, D50 of 89 μm and D90 of 156 μm. Average particle size of 100 μm.	Ti–6Al–4V	The microstructure includes prior β grains with length from 0.2 to 5 mm.		Higher tensile strengths are obtained along the orientations and wall structures which consist of a larger number of prior β grain boundary intercepts.	- UTS: 995–1118 MPa - Yield stress: 871–1015 MPa - Average elongation: 18%	[123]
Dinse push-push wire feeder. Kuka 6-axis robot	Trumpf YbYAG disk laser Used power: 5.5 kW	Wire	Ti–6Al–4V	The transformation of columnar prior β grains to globular β ones is reported.		The hardness and microstructure within the prior β grain are a function of the cooling rate, rather than of the duration temperatures above β-transus temperature.	- Hardness Vickers: 281-344	[112]
6-axis robot and a lateral wire-feeding device	Nd:YAG Used power: 3.5 kW	Wire	Ti–6Al–4V			No apparent relationship between the ductility or strength and the angle of fracture is found.	- Yield strength: 697–884 MPa - UTS: 790–960 MPa, - Elongation at failure: 5–12%	[55]
	Two 750W Nd:YAG lasers and one 14 kW CO_2 laser	GA Ti–6Al–4V powder	Ti–6Al–4V	The microstructure consists of columnar structures with average grain width of 120 μm (Nd:YAG) and 750 μm (CO_2).		Higher cooling rates (*i.e.*, a combination of low power and high speed) lead to thinner prior β-grains.		[74]
	Rofin CO_2 laser Used power: 7 kW	40–100 μm Ti–6Al–4V powder		The microstructure includes β-grains with Widmanstätten α-laths and needle-like martensitic α phase. Adiabatic shear bands are likely to be the source of crack initiation and propagation.	Voids and lack-of-fusion defects with 1–10 μm in diameter.	As for the tensile test, the flow stress at higher strain rates is lower than that at lower strain rates. Negative temperature impact on the flow stress under both compressive and tensile loading conditions is observed.		[30]
Weldaix wire-feeder and Kuka KR 100 6-axis robot	Trumpf HLD 3504 Nd:YAG diode laser Maximum power: 3.5 kW		Ti–6Al–4V	The microstructure within the prior β-grains consists of martensitic α′ and basket-weave α in the as-built and after the treatment at 600 °C for 4 h and furnace cooling.		While the heat treatment at 600 °C for 4 h and subsequent furnace cooling considerably increase the average hardness, the treatment at 1200 °C for 2 h followed by the furnace cooling remarkably decrease it.	- Vickers hardness: 308–343 HV	[110]
Optomec LENS® system	IPG fiber laser Laser power: 300W		Ti–6Al–4V			Measurement-based forced convection model achieves temperature errors less than 11%, while the free convection model errors are up to 44%.		[103]
5 axis Irepa Laser cladding system	Two different Nd-YAG laser sources Used powers: 2000W and 300W	45–78 μm GA powder	Ti–6Al–4V	Deposits in thin areas consist of orthogonal α′ martensitic laths, but thicker areas include Widmanstätten α+β lamellae structures.		Lower energy inputs lead to higher hardness (*i.e.*, 368 HV10) compared to the samples manufactured by lower energy inputs (*i.e.*, 357 and 333 HV10).	- Elongation at failure: 9%	[52]
		−150 to +150 mesh size powders	Ti–6Al–4V	The microstructure includes acicular secondary α phase and coarse primary α phase. Adiabatic shear bands including α twins are detected.	Initial elongated voids	Dynamic recrystallization is suggested to be the main deformation mechanism for the initiation and propagation of adiabatic shear bands. The heat treatment is shown to have a negative effect on the plasticity, but positive effect on the mechanical strength.	- Highest UTS for as-deposited specimens: 1600 MPa - Highest UTS for the heat-treated specimens: 1800 MPa	[109]

6 axis ABB robot	IPG YLR-6000 S fibre laser Used power: 6 kW	wire (1.14 mm in diameter)	The microstructure includes columnar prior β grains and colony α in the β grain boundaries.			Unlike the elongation at failure, higher UTS values for the transversal specimens were measured compared to longitudinal ones.	- Vickers hardness: 330 –342 HV - UTS: 900 MPa - Elongation at failure: 13%	[65]
			The microstructure includes the Widmanstätten structures.	Cavities, lack of bonding between layers and pores		The yield stress and UTS values of the Ti–6Al–4V samples are similar to those reported in the literature for the solution heat treated and aged components. Both the yield stress and the UTS of the flat Ti–6Al–4V samples are larger than those of the round ones, but the range of elongation to failure values is lower.	- Elongation at failure: 9.2–13.3 for round specimens and 3.4–10 for flat ones. - UTS: 935–989 MPa for round specimens and 1014–1085 MPa for flat ones. - Vickers hardness: 390 for thin walls and 363 for thick ones.	[79]
Precitec YC-50 cladding nozzle	IPG YLR-12000. Used power: 2 kW	89 μm average diameter PREP powder supplied by Timed Powder Metals	Ti–6Al–4V	The microstructure includes prior β grains oriented parallel to the building direction and grain boundary α at the prior β grain boundaries.	Lack-of-fusion pores	The presence of additional 0.0125 wt% oxygen in the Ti–6Al–4V component increases both the UTS and yield strength, but slightly reduces the ductility.	- Average UTS: 1060 MPa in both longitudinal and transversal directions. - Elongation at failure: 11% in longitudinal and 14% in transversal directions	[122]

decrease in the flow stress, known as "thermal softening" [109]. The plastic deformation at high strain rates is therefore controlled by the competition between the thermal softening caused by an adiabatic temperature rise and the work hardening resulting from the high values of the applied strain rate [109].

Several studies have reported the anisotropic mechanical properties of AM Ti–6Al–4V. High UTS values ranging from 900 to 1200 MPa have been reported for LMD Ti–6Al–4V [6,52,65,79,123]. Assuming that the transverse direction is defined as the one parallel to the build axis, the UTS values are 4% higher along the longitudinal direction as compared to the transverse direction. Similar levels of anisotropy are observed for the yield strength, where the values corresponding to the longitudinal direction are 2–5% higher than those along the transverse one [65]. This is also the case for the elongation at failure, where longitudinal specimens exhibit a much higher (*i.e.*, 18%) elongations at failure than the transversal ones do (i.e. 12%) [50,55,65,123,131]. The strain at failure strongly depends on the sample orientation too, where values up to 6% are obtained for non-treated specimens tested along their build direction [50]. Other authors have reported higher elongation values (*i.e.*, 10–15%) for non-treated specimens along the same direction [65,79,122]. The applied strain rate strongly influences these values. It has, for example, been found that LMD Ti–6Al–4V fails at lower stress values when the applied strain rate is higher [65,79,122]. An opposite effect is observed when the applied stresses are compressive with the flow stress (*i.e.*, the resistance to plastic deformation) increasing with the loading rate [65,79,122]. However, the above-mentioned trends are not necessarily generalizable and may be strongly dependent on the underlying microstructural features of the tested specimens. For instance, some studies have found that the elongation at failure for LMD Ti–6Al–4V components along the transversal direction may be 25–33% higher than those along the longitudinal one [65,123]. This is attributed to the presence of the lack-of-fusion porosities that are typically aligned perpendicular to the transverse direction. These pores result in lower ductility along the transverse direction [123]. The anisotropy of the mechanical properties may be also due to the elongated prior β grains that are usually observed in the microstructure of LMD Ti–6Al–4V components [49,107,122,123].

The mechanical properties of LMD Ti–6Al–4V also change with the distance from the substrate (Fig. 11). The regions close to the top surface of the component experience more convection and heat radiation to the surrounding air and shield gas, while the material closer to the substrate undergoes re-melting and its heat transfer is dominated by conduction [6]. In the transversal specimens, the tensile strength increases along the direction normal to the build plate, as the distance from the substrate increases. However, the regions with increased tensile strength experience lower elongations at failure [6]. Based on the orientations shown in Fig. 11, the mechanical properties of the specimens tested along the direction (001) are similar to those tested along the direction (010). On the contrary, the specimens tested in the direction (100) exhibit higher values of strength and elongation [6] (see Fig. 13).

6.2. Fracture toughness

For many metallic systems, ductile fracture occurs after extensive plastic deformation, necking, formation of small cavities, enlargement of cavities, and finally the fracture event that leaves behind a cup-and-cone shaped fracture surface. Brittle fracture is, however, characteirzed by minimal plastic deformation before the fracture event. Fracture toughness (K_{IC}) is the ability of flaw-containing materials to resist fracture. Depending on the processing conditions and the resulting microstructure and roughness, the fracture toughness of LMD Ti–6Al–4V components can be

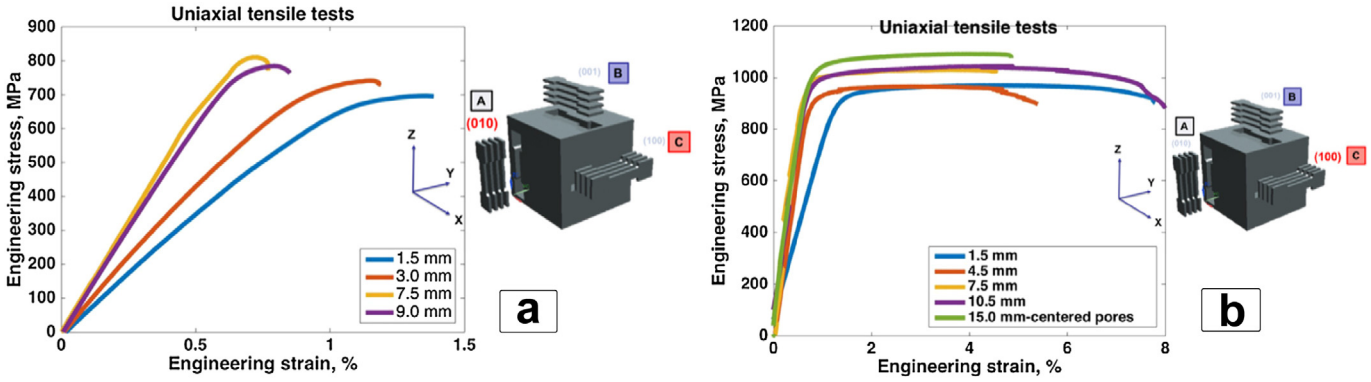

Fig. 11. The stress-strain curves of LMD Ti–6Al–4V for different specimen orientations and different distances from the surface of a cubic part: the directions (a) (010) and (b) (100) [6].

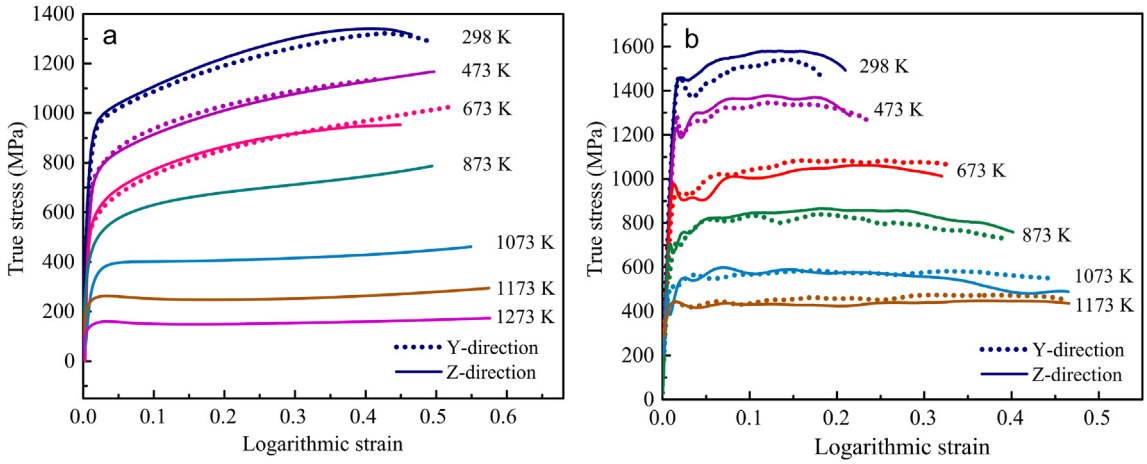

Fig. 12. The stress-strain curves of LMD Ti–6Al–4V parts. The tensile tests have been conducted along the *y* and *z* directions and under different temperatures and strain rates of (a) 0.1 s^{-1} and (b) 5000 s^{-1} [30].

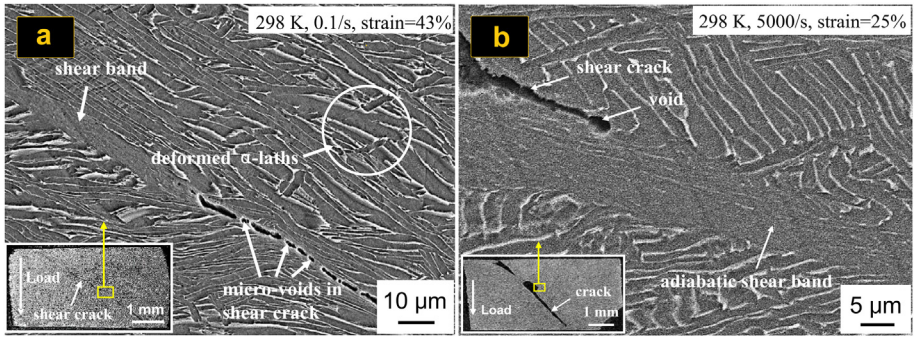

Fig. 13. The SEM images of LMD Ti–61Al–4V components showing shear failure under (a) a logarithmic strain of 43%, a temperature of 298 K and a strain rate of 0.1 s^{-1}, and (b) a logarithmic strain of 25%, a temperature of 298 K, and a strain rate of 5000 s^{-1} [30].

comparable with the values reported for conventionally manufactured counterparts. For example, Zhai et al. [76] found out that the fracture toughness of LMD Ti–6Al–4V parts are higher than their wrought counterparts, but close to EBM ones.

There is a general consensus that fracture occurring in adiabatic shear bands is not uniform and ultimate ruptures can result from both ductile and brittle fracture modes. Fracture usually starts by crack formation at preferential sites (*i.e.*, β grain boundaries). Due to the transversal orientation of the prior β grains, cracks cannot be easily detected on the cross-section of the fracture surface of longitudinal specimens. Susceptibility to adiabatic shear band localization increases after the material is subjected to heat treatments [65,109]. Both dimpled and smooth areas have been observed on the fracture surfaces of LMD Ti–6Al–4V parts (Fig. 14) [65,109].

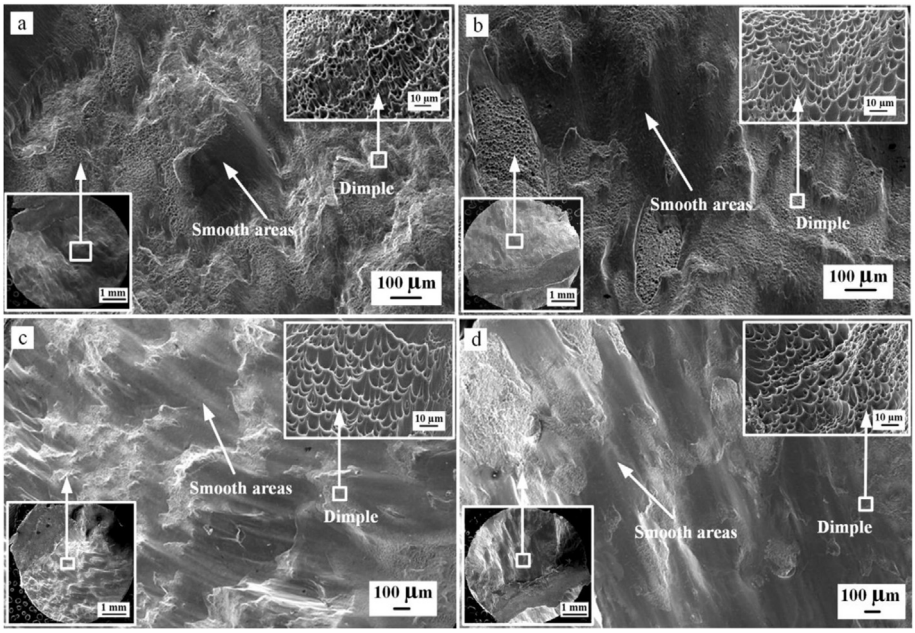

Fig. 14. The fracture surface of LMD Ti–6Al–4V parts after dynamic compression: (a) the as-deposited alloy tested under a strain rate of 1500 s^{-1}, (b) a heat-treated alloy tested under a strain rate of 1500 s^{-1}, (c) the as-deposited alloy tested under a strain rate of 3000 s^{-1}, and (d) a heat-treated alloy tested under a strain rate of 3000 s^{-1} [109].

Areas with dimples usually exhibit ductile fracture characteristics, while smooth areas exhibit the brittle type of fracture. Dimpled areas are formed as a consequence of higher plastic deformations before failure. Depending on the build directin of the specimen, different fracture surfaces can develop [65,109]. Transversal specimens generally show smoother cup-and-cone fracture surfaces, which is an indicator of a ductile fracture mechanism [65,109]. On the contrary, longitudinal specimens exhibit brittle type fractures [65,109]. The fracture surfaces of heat-treated specimens show larger smooth areas with fewer dimples when compared to the as-built ones [65,109]. Moreover, both the length and depth of dimples on the fracture surface of heat-treated specimens are shorter [65,109], revealing the relatively poor ductility of these materials.

Transmission electron microscopy (TEM) of the shear bands has revealed the deformation of twins of about 100–500 nm in size under quasi-static loading conditions [109]. At higher strain levels, however, these twins are absent and a high density of dislocations is observed [109]. The formation of ultrafine and equiaxed grains in metals with HCP structures is associated with dislocation slipping and twinning, which are proposed as the twining-induced rotational dynamic recrystallization mechanisms [109]. These dynamic recrystallization-induced tiny grains are thought to be accompanied by a sudden reduction in the dislocation density, which leads to instant softening [109]. In conclusion, twining-induced rotational dynamic recrystallization is considered to be the main deformation mechanism for the initiation and propagation of adiabatic shear bands in heat-treated LMD Ti–6Al–4V subjected to dynamic loading [109].

The hardness of LMD Ti–6Al–4V strongly depends on its thermal history (*i.e.*, temperature, cooling rate, and heat accumulation). The thermal history can be manipulated by variations in the process parameters and incident energy density. For example, Paydas et al. [52] have studied the relationship between the microstructure and hardness of LMD Ti–6Al–4V. The harder zones of the material (*i.e.*, 350–370 HV10) were related to the martensitic microstructure formed after rapid cooling. Softer areas (*i.e.*, 315–350 HV10) corresponded to the Widmanstätten structure formed at the lower cooling rates [52]. The hardness and microstructure in a prior β grain is a function of the rate at which the material has been cooled to temperatures below the β-transus temperature rather than of the time duration it has been kept at temperatures above the β-transus temperature [112]. For example, heating at 600 °C for 4 h and a subsequent furnace cooling heat treatment have been found to not significantly influence the microstructure of the material but to increase its average hardness [50]. Inversely, a solution heat treatment at 1200 °C for 2 h, followed by furnace cooling, has been found to substantially decrease the hardness values [50]. The increase in the hardness may be a result of the $Ti_3Al(\alpha_2)$ precipitation [50].

6.3. Fatigue behavior

In many practical applications, LMD parts are subjected to cyclic loading that might cause fatigue failure. Fatigue tests are usually performed according to the ASTM standard E606-92 or similar standards. The test results are highly influenced by the porosity content and the microstructure of the components, the latter being dependent on the cooling rate during the deposition [42]. Generally, if the fatigue test is performed below 10^3 cycles, it is considered to be a low cycle fatigue (LCF) test, while fatigue tests with more than 10^5 of loading cycles are considered high cycle fatigue (HCF) tests [31]. When evaluating the fatigue behavior of LMD components, pore shape, size, location, and quantity should be considered. As compared to wrought materials, the lack-of-fusion porosity usually leads to lower values of the fatigue strength and fracture toughness [115]. However, HIP has been proven to be a useful technique for reducing the lack-of-fusion pores [115]. The nucleation and propagation of initial cracks usually occurs through pores. It is therefore crucial to optimize the processing parameters such that the number and volume of the pores are minimized in the resulting LMD parts. From the data presented in Table 5 regarding the fatigue properties of SLM, LMD, EBM, and conventionally manufactured Ti–6Al–4V, it can be concluded that despite the large scatter of the fatigue data, the fatigue properties of LMD

Table 5
A brief list of the fatigue properties reported for the SLM, LMD, EBM, and conventionally manufactured Ti–6Al–4V alloy.

Fabrication method and post treatments	Frequency	R value	Fatigue strength (MPa)	Ref.
SLM	20 Hz	−0.2	100–120	[33]
SLM	20 Hz	0	30–150	[4]
SLM	50 Hz	0.1	200	[159]
SLM	19 kHz	−1	300	[261]
SLM	19 kHz	−1	230	[262]
SLM	115 Hz	−1	200	[263]
Casting	10 Hz	0.1	360	[264]
Powder metallurgy	50 Hz	−1	222	[265]
Powder metallurgy	10 Hz	−1	100	[266]
Powder metallurgy	–	–	500	[267]
LMD	100 Hz	0.1	770	[50]
EBM	–	0.1	200–250	[268]
EBM	20–120 Hz	0.1	200–300	[269]
EBM	–	0.1	150	[7]
DMLS	–	0.1	200	[7]

Ti–6Al–4V are much better than those reported for cast parts and similar to or better than those reported for the wrought materials. Similar to the case of SLM Ti–6Al–4V, wire-fed LMD Ti–6Al–4V components are reported to exhibit HCF lives equal or better than those measured for wrought Ti–6Al–4V. In comparison, EBM Ti–6Al–4V specimens exhibit significantly lower fatigue strengths when compared to their wrought counterparts [42].

The range of the stress values applied during fatigue tests is limited, as they should be below the yield strength of the material to ensure no plastic deformation takes place (DeutscheNorm, 1978) while being large enough to allow for finding the endurance limit within a reasonable amount of testing time [50]. The controlling factor in a HCF test is the resistance to crack nucleation, whereas in LCF, the resistance to the propagation of small surface cracks (*i.e.*, micro-cracks) is crucial [31]. HCF specimens are often tested according to DIN 50100. Colony boundaries as well as martensitic plates are strong impediments to the propagation of micro-cracks [132]. Therefore, the LCF strength generally improves with the cooling rate (*i.e.*, a decreasing colony size). Moreover, larger α grain sizes usually decrease the fatigue resistance [31].

The fatigue properties of LMD Ti–6Al–4V have been also found to be anisotropic. In particular, fatigue specimens taken from the transversal direction usually exhibit lower fatigue limits than those taken from the longitudinal direction [133,134]. Baufeld et al. [50] have reported fatigue limits of about 870 MPa at 1.3×10^7 cycles after an annealing heat treatment of 843 °C for 2 h, followed by furnace cooling. Kobryn et al. [74] have reported the beneficial effects of HIP on the anisotropic fatigue behavior of LMD Ti–6Al–4V. In the same study, the specimens subjected to stress-relief treatments (for 2 h at 700–730 °C) exhibited lower fatigue strengths as compared to the wrought or HIP ones. A lower fatigue strength limit as compared to the wrought counterparts is reported in Ref. [42] too.

The fatigue crack growth rate (FCGR) is usually determined under the fatigue tests performed according to the ASTM E647 standard. It has been demonstrated that LMD Ti–6Al–4V parts built in the transversal direction have higher crack growth resistance in both as-built and stress-relieved conditions than the longitudinal specimens [135]. Moreover, a higher scanning speed results in lower values of the FCGR [135]. In general, LMD Ti–6Al–4V components have lower FCGR values than the SLM ones. The crack initiation in LMD parts is slower than that of SLM ones [135]. For example, at a stress intensity of 12 M Pa.m$^{1/2}$, the FCGR is around 10^{-8} m/cycle for LMD parts, while it is 10 times higher for the SLM ones. This crack initiation behavior is linked to larger values of the laser spot size in LMD as compared to SLM, which results in much lower scanning speeds (around 1 m/min) and, thus, much lower cooling rates and reduced residual stresses [135].

6.4. Surface roughness

As compared to other AM processes such as SLM, LMD results in a lower quality of the surface finish. Indeed, surface roughness values in the range of Ra 4 to Ra 200 have been reported for LMD Ti–6Al–4V, while the roughness of SLM parts vary between Ra 5 and Ra 10 [49,136]. The deposited layers and their accompanying curved layer bonds are macroscopically visible in LMD. The surface roughness of LMD parts tends to increase with the powder flow rate [49,136]. Moreover, the technology used for the production of the powder material can significantly influence the surface roughness in LMD [49]. For example, the surface roughness of the parts made from GA powders is higher than that of the ones realized using PREP-processed powder (Fig. 15) [49].

6.5. Measurement of the residual micro-strains and stresses

The thermal stresses induced during the LMD process give rise to residual stresses that adversely affect the mechanical properties and geometrical accuracy of LMD parts [42,137,138]. It is therefore necessary to limit the magnitude of the residual stresses either by optimizing the processing parameters [139,140] or by pre-heating the substrate [141].

There are a number of destructive (*e.g.,* sectioning [142], hole [143], and deep hole drilling [144,145]) and non-destructive (*e.g.,* x-ray or neutron diffraction [146], ultrasonic methods, and magnetic methods [147]) methods available for the measurement of the residual micro-strains and stresses developed in the components. The micro-strains characterize the defects in the form of composition gradients and stacking faults in the structure. Dislocations are the largest source of micro-strains particularly in ductile materials. The micro-strains can be measured using the characteristics of the diffraction angle [148]. Measuring the micro-strains at different levels can be used for the calculation of the principal residual stresses in the structure. The outputs of such an analysis can be used to evaluate the quality of the surfaces.

Among non-destructive methods, neutron diffraction has been used before for the measurement of the residual stresses developed in LMD Ti–6Al–4V [149]. The neutron diffraction methods are based on the variation in diffraction angles, which originate from the zones experiencing compression or tension. There are empirical relationships for the calculation of the average strains in the gauge volume based on the direction and particular {hkl} crystallographic planes as [150]:

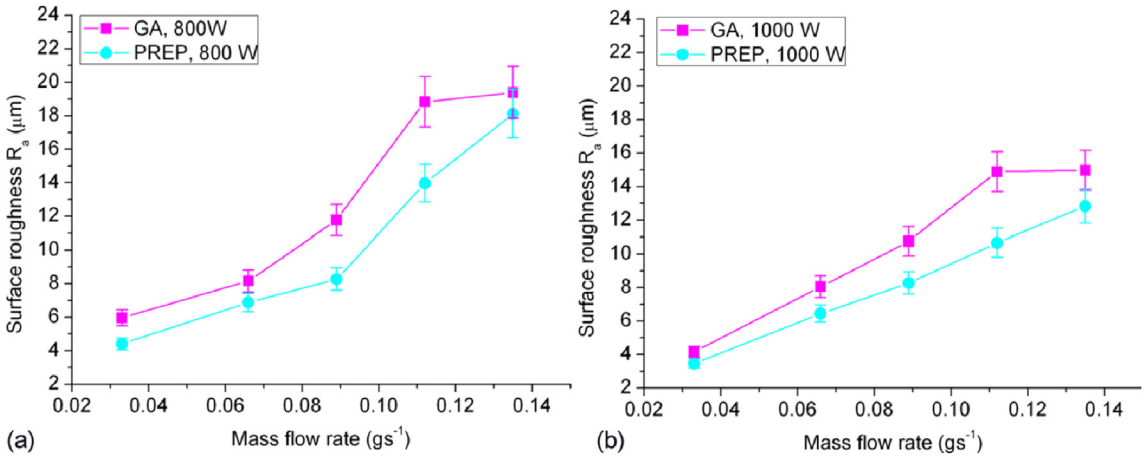

Fig. 15. The surface roughness of GA and PREP-processed powders as a function of the mass flow rate and laser power [49].

$$\varepsilon_{hkl} = \frac{d_{hkl} - d_{0,hkl}}{d_{0,hkl}} = \frac{\sin\theta_{0,hkl}}{\sin\theta_{hkl}} - 1 \quad (2)$$

where d_{hkl} is the lattice plane spacing and θ_{hkl} is the angle between the scattering plane {hkl} and the incident beam. $\theta_{0,hkl}$ and $d_{0,hkl}$ are the reference values for stress-free lattices. The calculated strains can be converted into the local values of the residual stress using the Hook's law.

Computational simulation is another approach for evaluating the residual stresses developed in LMD Ti–6Al–4V. When deciding about the processing parameters, such *a priori* simulations can be used to avoid locations with high residual stresses [151].

7. Process-microstructure-property relationships

Throughout this paper, we have discussed the relationships between the processing parameters, microstructure, and the physicomechanical properties of LMD Ti–6Al–4V alloy. However, it is useful to summarize the ways through which the processing parameters and microstructural features can affect the mechanical properties of LMD parts. In this section, we present a deeper overview of the process-microstructure-property relationships in LMD Ti–6Al–4V.

7.1. Effects of build geometry and direction

As previously discussed, LMD components undergo rapid melting and solidification with complex thermal histories, resulting in inherently anisotropic microstructures and properties. The mechanical properties of LMD parts are therefore dependent on the build plan and direction. It is crucial to understand the anisotropy phenomenon and its complex relationship with the LMD parameters to successfully tailor the LMD process for the desired mechanical properties [6,122]. Generally, the anisotropy in the mechanical properties of LMD Ti–6Al–4V components arises from the following two microstructural phenomena, apparently inherent to the process:

7.1.1. Lack-of-fusion porosity

The lack-of-fusion porosities usually appear between the deposited layers due to the inability of the melted material to fill the gap between the subsequent layers. This reduces the mechanical properties of the resulting LMD material including its strength and total elongation along the *z* direction (*i.e.*, the build direction) in comparison with those in the *x* and *y* directions (*i.e.*, the scanning directions) [152–155]. These pores affect the anisotropy of the resulting material more than the other types of pores do (*e.g.*, the ones caused by gas entrapment), because they are primarily oriented vertical to the build direction [6].

7.1.2. Elongated prior β grains

The microstructure of LMD Ti–6Al–4V components usually consists of large elongated prior β grains growing towards the heat source (*i.e.*, the build or z-direction). Therefore, measuring the properties along the build direction means performing the tests almost parallel to the elongated prior β grain boundaries [65,122] (Fig. 16a). Such a grain orientation results in lower volume fractions of grain boundaries in a specimen fabricated along the build direction than those made along the scanning direction (Fig. 16b) [65,122]. Some studies have indicated that these boundaries serve as the potential sites of failure initiation and significantly reduce the elongation in the scanning direction as compared to the build direction [21,50,65,107,156–158]. That is due to the fact that the prior β grain boundaries are normal to the tensile stress and act as opening mode cracks (Fig. 16d). In the *z*-direction, however, the prior β grain boundaries are parallel to the tensile load, resulting in safer conditions [65]. More interestingly, the existence of a large population of grain boundaries in the specimens oriented along the *x*-direction results in higher values of the tensile strength [65] due to the Hall-Petch relationship [123]. Such types of anisotropy typically amount to 25–33% of the total tensile elongation and 2–5% of the tensile strength [65].

Moreover, the location of the tensile test specimen is one of the most significant factors influencing the measured mechanical properties, because each point of the LMD component undergoes a specific cooling rate and has its own thermal history. In general, the tensile specimens located closer to the superficial regions of the LMD part experience more heat transfer with the surrounding air through convention and radiation, while the material located at the central regions undergoes re-melting and is limited to conduction for the transfer of its heat. This is the reason why the yield and tensile strength values increase and the elongation at failure decreases when moving from the central regions of LMD components towards their peripherical locations. Similar observations have been made by Keist et al. [123]. Accordingly, the variation in the α lath size (higher values at the top regions) may play an important role in creating such a gradient in the mechanical properties [123]. On the other hand, Baufeld et al. [50] have observed a reverse trend. They found out that the top regions of a LMD Ti–6Al4V component

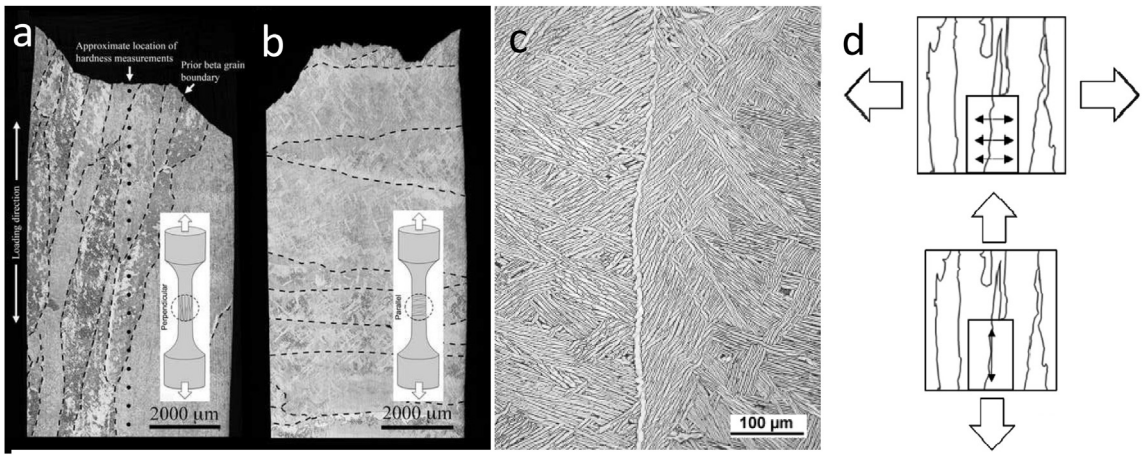

Fig. 16. Some optical micrographs of a number of tensile test specimens made from LMD Ti–6Al–4V that are eithe (a) perpendicular and (b) parallel to the scanning direction. (c) The typical appearance of the grain boundary α phase along the prior β grain boundaries [65] and (d) a schematic illustration of the force applied along the grain boundary α [122].

exhibit higher values of the tensile strength due to the microstructural variations caused by different cooling rates. High cooling rates in the top regions may result in unique microstructures with higher hardness and strength caused by the dislocation or solid solution hardening mechanisms. Optimizing the geometry [123] and build plan [66] can therefore decrease the degree of anisotropy in the mechanical properties of LMD parts and enhance the reliability and reproducibility of this AM process.

7.2. Effects of post-AM heat treatments

Since melting, heterogeneous nucleation, and rapid solidification phenomena are all present in the LMD process, the resulting microstructural features have a close relationship with those found in cast or welded parts. On the other hand, the fine lamellar structures and martensitic phases that form in LMD Ti–6Al–4V components due to high cooling rates endow the fabricated parts with superior mechanical properties comparable to those of wrought alloys. The formation of such microstructures, however, greatly decreases the ductility of the material. As a result, an appropriate post-AM heat treatment may need to be applied to enhance the ductility or strength of the material and make sure its mechanical properties are uniformly distributed and are comparable to those observed for wrought parts [55,109,159–162].

The heat treatments of LMD Ti–6Al–4V components can be carried out either below or above the β-transus temperature. Subtransus heat treatments change the morphology, microstructure, and size distribution of α and martensitic phases, but do not significantly influence the prior β grains [74,110]. For instance, the martensitic α′ phase may be transformed into lamellar α + β phases. In the case of supertransus heat treatments, however, the prior β grains undergo excessive grain growth and phase transformation into lamellar α+β phases [163,164]. Supertransus heat treatment are, nevertheless, associated with certain problems such as the complete dissolution of the α phases, high energy consumptions, handling problems, excessive grain coarsening, and the embrittlement of the surface layers [112]. Interestingly, furnace cooling after heat treatments at higher temperatures (*e.g.*,1200 °C) may lead to the transformation of the elongated prior β grains into equiaxed ones [55,112]. Due to the high tendency of titanium to chemically react with oxygen and nitrogen, post-AM heat treatments are usually carried out under an inert atmosphere [164,165].

Grain growth, coarsening of the lamellar structures, and stress relief are among the most common phenomena occurring during the post-AM heat treatments of LMD Ti–6Al–4V, giving rise to the lower strengths and higher levels of ductility [55,157]. Some studies [55,157], however, report no change or even an increase in the strength as a result of post-AM heat treatments. It is believed that these observations are results of the competition between the following phenomena.

7.2.1. Transformation of martensitic phase to lamellar α+β

Although it is generally accepted that the conversion of the martensitic phase to the α+β phase reduces the strength and increases the ductility of the material [109], Brandl et al. [157] have found out that such a transformation may result in slight increase in the tensile strength due to the formation of more α content and the increase of the α to β ratio. According to their findings, since the α phase has a higher strength than the β phase, a higher fraction of α after the applied heat treatment compensates the strength reduction caused by the coarsening of the lamellar structure and stress relief.

7.2.2. Re-sintering

The applied heat treatments can increase the tensile strength by reducing the internal porosity of the material through re-sintering [166].

7.2.3. Precipitation hardening

Precipitation hardening has been observed in the post-AM heat treatments of LMD Ti–6Al–4V components at 600 °C for 4 h followed by furnace cooling [55,157]. At this temperature, coherent Ti_3Al precipitates may form inside the α phase due to significant levels of partitioning of the alloying element and the enrichment of the α-stabilizing elements (*i.e.*, Sn, O, Al). At temperatures above 600 °C, however, the Ti_3Al particles start to dissolve [55]. Since the precipitation process is exceedingly slow, a low cooling rate is required to ensure that these phases are precipitated. In addition to the positive effects of the Ti_3Al precipitates on the mechanical strength of LMD Ti–6Al–4V, they can decrease the ductility of the material [55]. Table 6 presents a summary of the microstructural phenomena and their effects on the physicomechanical properties of LMD Ti–6Al–4V components after different types of post-AM heat treatment cycles.

7.3. Effects of porosity content

As previously discussed, two types of undesired porosities are

Table 6
The effects of post-AM heat treatments on the microstructure and physicomechanical properties of LMD Ti–6Al–4V.

Heat-treatment cycle	Effects on Microstructure	Effects on physicomechanical properties	Ref.
600 °C/4h	- It does not lead to the coarsening or significant change in the microstructure.	- No apparent effect on tensile properties.	[50]
843 °C/2h	- It does not lead to the coarsening or significant change in the microstructure.	- No apparent effect on UTS. - Significant increment in the elongation at failure in the scan direction.	[50]
600 °C/4h-Furnace cooling	- It leads to the precipitation of coherent Ti3Al particles.	- No effect on hardness. - Significant Increment in tensile strength in both x and z directions. - Increment in total tensile elongation in the x direction.	[157]
843 °C/2h- Furnace cooling	- It leads to the microstructure coarsening, grain growth, and stress relieving (*i.e.*, reduction in the number of dislocations).	- No effect on hardness. - Slight Increment in tensile strength in both x and z direction. - Increment in total tensile elongation in the scan direction.	[157]
600 °C/4h-Furnace cooling	- It leads to the precipitation of coherent Ti_3Al particles.	- Increment in strength and reduction in ductility.	[157]
843 °C/2h-Furnace cooling	- It leads to the microstructure coarsening, grain growth, and stress relieving (*i.e.*, reduction in the number of dislocations).	- Increment in total tensile elongation. - Not large effect on the tensile strength.	[157]
1223k/4h-Air cooling-aging at 873k/2h	- Primary α phase grains get coarsened. - Secondary acicular α forms inside the primary β phase.	- Decrement in plasticity. - Increment in strength.	[109]
600 °C/4h	- It leads to the precipitation of coherent Ti_3Al particles.	- Significant increment in tensile strength in deposition *i.e.*, z-direction. - Decrement in ductility.	[55]
1200 °C/2h	- Elongated β grains are transformed into equiaxed ones. - Large α colonies begin to form. - The number of dislocations starts decreasing. - The Lamellar structure is coarsened.	- Decrement in tensile strength.	[55]
760 °C/1h- Air cooling	- The martensitic α′ transforms into fine α+β microstructure, during which new β phase forms between martensitic plates as a continuous layer.	- Decrement in tensile strength and increment in ductility	[115]
843 °C/2h- Furnace cooling	—	- Increment in ductility and decrement in tensile strength	[156]

often present in LMD components including initial voids and the lack-of-fusion pores. The initial voids have regular smooth shapes (*e.g.*, a sphere) with smooth inwalls [167]. They are randomly distributed within the fabricated component and are caused either by gas entrapment during melting and solidification or by gaseous impurities in the feedstock powder [167]. The lack-of-fusion pores usually form between two subsequent deposited layers or between the first deposited layer and the substrate due to the incomplete stacking of the layers caused by non-molten powders. At sufficient temperature, low laser power, or a high powder feeding rate may lead to incomplete melting of the powders and the formation of the lack-of-fusion pores. These pores have irregular shapes with coarse inwalls [30,122,168,169].

These defects play important roles in determining the mechanical properties of LMD Ti–6Al–4V. A number of microscopic studies have revealed that the formation of adiabatic shear bands during compression tests is the main source of failure in Ti–6Al–4V parts. The aforementioned defects can serve as nucleation sites for the formation of adiabatic shear bands (Fig. 17a) and as a source for crack initiation and propagation (Fig. 17b). Since the excessive heat generated during compression tests cannot escape within a short time, the voids may be the best sites for releasing the heat [30]. Microcracks can therefore evolve from the voids and form shear bands [30].

Similar to the case of compressive stresses, the lack-of-fusion pores and initial voids can degrade the tensile strength and ductility of LMD Ti–6Al–4V parts. They usually grow and expand under tensile loads, resulting in lower tensile strengths in comparison to the compressive strengths of the same system. Moreover, their sharp tips act as stress concentration sites, thereby promoting crack initiation and propagation [30].

As compared to the tensile and compressive strengths, the

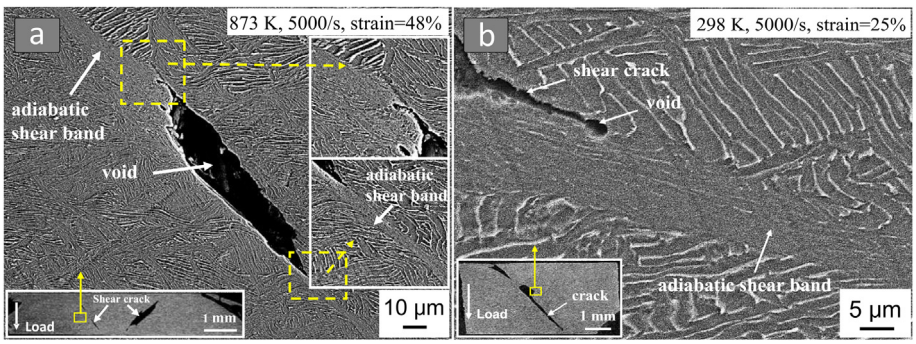

Fig. 17. Some SEM images of LMD Ti–6Al–4V compressive test specimens depicting (a) an adiabatic shear band and (b) a shear crack initiated from the tip of a void [30].

fatigue behavior of LMD Ti–6Al–4V parts is more sensitive to the presence of the initial voids and the lack-of-fusion pores [116,170]. Sterling et al. [42] have stipulated a meaningful relationship between these defects and the elongation at failure according to which the larger the population of the structural defects, the lower the elongation at failure and the shorter the fatigue life.

When compared to round-shape voids, the angular pores are more detrimental to the fatigue resistance of the material due to the stress concentration present at sharp tips [30,42]. The pore size and its shape irregularity can therefore also affect the fatigue behavior of LMD Ti–6Al–4V. Generally, pores with a higher degree of irregularity, larger size, and a shorter distance from the outer surface are more detrimental to the fatigue behavior [42]. There is, however, a weak correlation between the fatigue life and the total number of pores [42]. More interestingly, a shorter distance between the pores results in a shorter fatigue life, probably due to easier crack propagation [42].

To improve the mechanical properties of LMD Ti–6Al–4V components by reducing their porosity content, one needs to optimize the processing parameters or apply appropriate post-AM heat treatments. For instance, Sterling et al. [42] have observed a significant improvement in the fatigue resistance after the application of an appropriate heat treatment. This strategy reduces the porosity content such that the fatigue behavior is no longer dominated by the effects of the pores but by the specifications of the α-colony boundaries (*i.e.,* the texture of the material).

7.4. Effects of surface roughness

In most cases, the surface roughness of LMD metallic components arises from the partial melting of the powder as well as the layer-by-layer nature of the fabrication process [171]. The surface roughness degrades the total elongation more in the vertical (*i.e.*, *z* or build direction) tensile test specimens than in the horizontal (*i.e.*, *x* or scanning direction) ones, because the superficial extrusions and the steps emerging at the end of the stacked layers are vertically aligned to the tensile stress in the *z*-direction and generate mode I loading conditions.

One way to reduce the surface roughness of LMD parts and to enhance their mechanical properties is machining [154,172], as demonstrated by Wilson-Heid et al. [172]. They observed that machining could enhance the elongation at failure from 6.5 to 7.8% by lowering the surface roughness. Machining could also alleviate the residual stresses present at the surface of LMD Ti–6Al–4V components, thereby improving their mechanical behavior [31]. Another approach that removes the necessity for post-AM machining has been proposed by Gharbi et al. [173]. They found out that the surface roughness usually originates from two physical phenomena, namely the unmolten powder present on the surface and the formation of menisci with pronounced radii of curvature in the melt pool. They proposed that using thin additive layers combined with large melt pools (formed by higher laser powers) improves the mechanical properties of the resulting part through a decreased surface roughness.

7.5. Effects of post-LMD thermomechanical procedures

In addition to post-AM heat treatments and machining, HIP has been used as an appropriate post-LMD thermomechanical procedure to improve the ductility and total elongation of LMD Ti–6Al–4V parts. HIP can effectively reduce the porosity content, increase the relative density, and enhance the total ductility, elongation, and fatigue behavior of AM parts by applying elevated temperatures and isostatic pressures [31,129,152,165]. However, HIP may coarsen the α phase platelets (lathes), thereby decreasing the tensile strength. The coarsening of the α phase platelets reduces their contribution to the Hall-Petch strengthening phenomenon [31,129,152,165]. This underlines the importance of optimizing the parameters of the HIP treatment to ensure a good balance between the strength and ductility is achieved.

7.6. Effects of the oxygen content

Ti–6Al–4V has a high tendency to chemically react with oxygen and nitrogen. As a result, much effort should be done in the LMD process to prevent the oxidation of this alloy and to control its oxygen content. Overall, oxygen atoms are located in the interstitial sites of the Ti–6Al–4V lattice, resulting in higher strengths due to their strengthening effects and the stabilization of the α phase. However, if the oxygen concentration exceeds a critical value, the ductility usually diminishes [174–176]. This is why controlling the oxygen level of the finished part is crucial for obtaining a good combination of strength and ductility. The oxygen present in finished LMD Ti–6Al–4V components typically originates from the oxygen dissolved in initial powder and the oxygen entrapped in the part during its various steps of handling and processing [122,123,177].

7.7. Effects of processing parameters

The melting and solidification processes as well as the local thermal history of LMD parts strongly depend on the processing parameters such as the laser power and scanning speed [10,74,178]. One therefore has to optimize the processing conditions to achieve finished parts with the desired properties [179].

7.7.1. Laser power

A higher laser power usually translates into a higher energy input and a lower cooling rate, giving rise to larger grain sizes, coarser columnar grains, and lamellas. The large grains can decrease the strength and hardness of the component [180]. Moreover, higher laser powers decrease the volume fraction of the martensitic phase due to lower cooling rates, thereby improving the ductility and fatigue behavior of the material but reducing its tensile strength [115].

7.7.2. Powder (wire) feed rate

The amount of powder or wire that is fed to the melt pool determines the layer thickness and affects the resulting microstructure. Increasing the powder (wire) feed rate results in a thicker layer and a coarser microstructure, thereby decreasing the strength and increasing the ductility of LMD Ti–6Al–4V parts [31]. The scanning direction and the feed rate of the shielding gas control the rate of powder injection too, meaning that they could also affect the mechanical properties of LMD parts [31]. A combination of a high laser power and a low feed rate has been found to effectively suppress the generation of the lack-of-fusion pores by ensuring the full melting of the powder (or wire) [129].

7.7.3. Scanning speed

In general, increasing the scanning speed or decreasing the incident energy sharpens the thermal gradient and raises the cooling rate [180,181]. This may lead to the refinement of the lamellar structures and the evolution of a finer microstructure with a higher volume fraction of the martensitic phase, dislocations, and grain boundaries, thereby enhancing the hardens of the resulting

material [180,181]. Using very high scanning speeds may, however, decrease the bonding between the deposited layers and consequently reduce the mechanical properties [10]. A lower scanning speed also prolongs the interaction time between the metal and laser, resulting in a larger melt pool. Moreover, the material remains at elevated temperatures for a longer time, leading to grain coarsening and decreased mechanical properties [182].

8. Applications in aerospace and biomedical industries

Due to the high specific strength and excellent formability of Ti–6Al–4V, this material has a wide range of applications in the aerospace industry. Indeed, one of the key applications of the LMD process is the repair of the Ti–6Al–4V parts used in the aerospace industry [183]. For such purposes, a combination of different manufacturing techniques (*e.g.*, LMD and machining) can be utilized [184]. Such integration can enhance the mechanical properties of the damaged parts. An LMD process with optimized processing parameters could be also used for the fabrication of very large parts without introducing geometrical distortions. This is a very attractive solution for the fabrication of the parts made from high quality and high performance materials for applications in the aerospace industry [129]. Recently, the French LMD company BeAM has partnered with PFW aerospace to qualify a LMD Ti–6Al–4V component for use in a large civil passenger aircraft [185].

Ti–6Al–4V also exhibits a good level of biocompatibility, high corrosion resistance, and low stiffness. It can therefore be used for the fabrication of AM porous orthopaedic implants using SLM [186], EBM [187,188], or LMD [189]. Exploiting the form-freedom offered by AM processes, one can precisely control the interconnectivity and spacing of cellular lattices, thereby adjusting their mass transport properties (*e.g.,* permeability [190,191]) as an important factor influencing bony ingrowth. The ingrowth of the bony tissue into the open porous structures can ultimately result in improved implant fixation and, thus, improved implant longevity [192,193]. An increased surface area is the other advantage of this AM porous biomaterials that can be later used for bio-functionalization processes [194–196]. Moreover, patient-specific medical devices could be realized using AM processes [32].

9. Cellular structures

AM processes can be used for the fabrication of lattice structures with complex micro-architectural designs. However, this capability is usually limited to open-cell cellular structures where the removal of the excess powder is relatively straigthforward. The design of such metallic lattices may vary between uniform structures made from one single repeating unit cell to heterogeneous lattices made of multiple types of unit cells with graded or irregular shapes [197–200]. The geometry of such AM cellular structures may have been designed using a CAD-based, an image-based, or an implicit surface modeling approach or be the direct output of a topology optimization algorithm [32,201–203].

Cellular structures with various types of micro-architectural designs have a wide range of applications in many engineering fields such as aerospace and bioengineering due to their unique mechanical properties [204–206]. An important example is the fabrication of orthopaedic implants and bone substitutes where the interconnectivity and spacing of porous biomaterials could be precisely controlled using custom-made or patient-specific designs originating from clinical images [207]. This is an essential aspect, because proper geometrical design can enhance the bone regeneration performance of implants and increase their longevity [191,208–210]. Moreover, given the fact that the topological design of AM cellular structures can directly control their physical and mechanical properties [32], the mechanical properties of such porous biomaterials can be adjusted such that they are as close as possible to the mechanical properties of the tissues they replace, thereby minimizing the effects of the stress-shielding phenomenon (Fig. 18a–c) [211,212].

Among different metals and alloys used for fabrication of AM porous biomaterials, Ti–6Al–4V is one of the most well studied materials because of its excellent biocompatibility, high levels of corrosion and wear resistance as well as high specific strength [213]. AM Ti–6Al–4V porous biomaterials have been fabricated using various types of AM processes in the past including SLM [214–217], EBM [218–220], and LMD [221,222]. The number of studies on LMD porous biomaterials is, however, limited as compared to the powder bed fusion techniques, perhaps due to the intrinsic limitations of the LMD process for the fabrication of lattice strucutres with precisely controlled geometries. In general, LMD porous biomaterials exhibit a lower surface quality, a lower accuracy, and a lower resolution, while the main advantage of LMD is in the repair of already existing parts [205,223–227]. Moreover, LMD materials usually require post-treatments such as surface treatments, milling, and stress relief processes to reduce the residual stresses and increase the quality of the material [224]. These processes increase the production time and cost.

Furthermore, cellular structures can be used for the fabrication of mechanical metamaterials, which are a class of advanced engineering materials with unusual macroscopic properties that originate from their design at a smaller scale [228–230]. Some of these unusual properties include a negative Poisson's ratio (also known as auxetic behavior) [231,232], a negative thermal expansion [233,234], and acoustic cloaking [235,236]. Metamaterials can be made from polymers [237–240], metals, or alloys [241,242]. There are some examples of mechanical metamaterials made from Ti–6Al–4V in the literature where tuning the topological design of lattices (*i.e.,* using stretch-dominated unit cells, bending-dominated unit cells, or a combination of both) has allowed researchers to obtain unusual mechanical properties. These unusual properties include a high energy absorption rate realized through honeycomb-like lattices (Fig. 1d and e) [243], a high bulk modulus together with a negligible shear resistance obtained using pentamode like unit cells [244], a robust mechanical performance achieved using octet-truss lattices [245], and tunable thermal-mechanical properties resulting from the use of octet lattice bimaterials (Al6061–Ti–6Al–4V) [246]. LMD allows for fabricating complex topological designs from multiple materials [247], which is a unique opportunity for designers to create metamaterials with advanced functionalities and uqniue properties.

10. Conclusions and future research

We presented an overview of LMD as one of the most common AM techniques for the fabrication of Ti–6Al–4V components with a focus on the relevant processing parameters, microstructures, heat treatments, and mechanical properties. We addressed the following critical subjects:

i. The processing parameters of LMD strongly affect the cooling rate and the thermal gradients in the melt pool. The thermal history of LMD Ti–6Al–4V parts governs their solidification behaviors, microstructures, porosity contents, and the distribution of the resulting residual stresses.

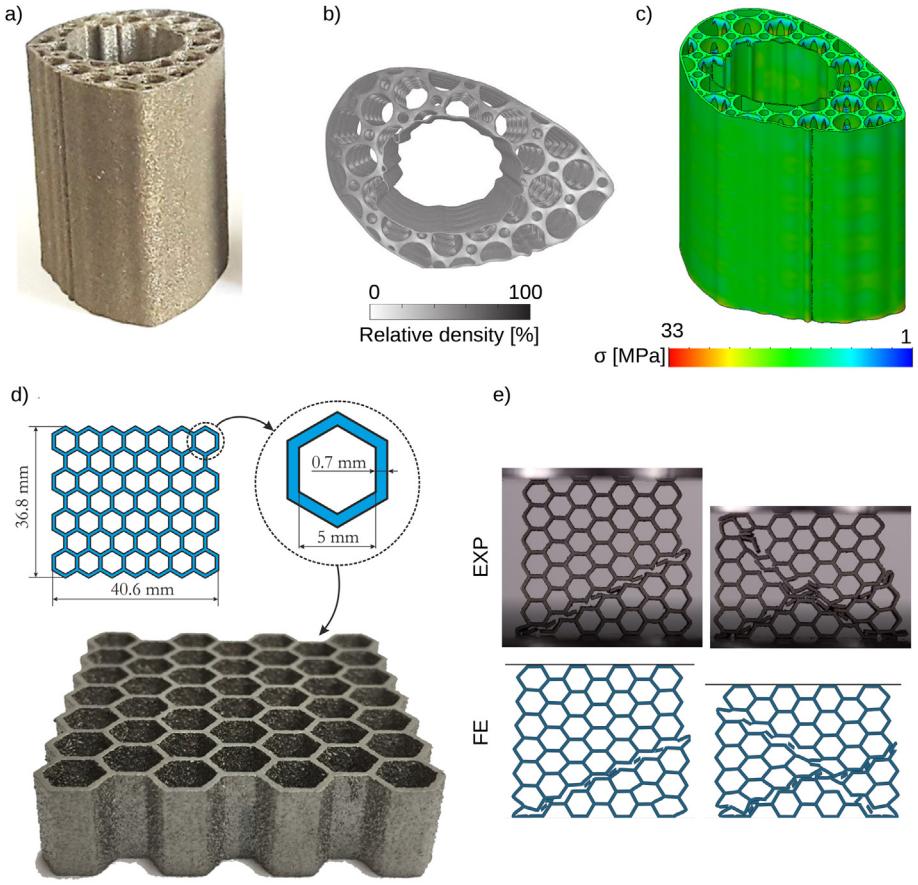

Fig. 18. (A) An example of DMLS implant prototypes made from Ti–6Al–4V [222], (b) the micro-architecture of the cellular structures that have been designed to match the stiffness of the native bone and to reduce the stress shielding phenomenon in the treatment of segmental bone defects [222], (c) the distribution of the von Mises stress calculated using computational models, showing some regions with high levels of stress concentrations [222], (d) an example of some honeycomb-like lattice structures made from Ti–6Al–4V using LENS™ [243], and (e) the lattice structure shown in Fig. 17d that is mechanically tested and numerically simulated [243].

ii. The tensile and fatigue properties of LMD Ti–6Al–4V parts strongly depend on the microstructure developed during the fabrication process. Defects such as pores or cracks are often present in LMD parts, resulting in lower levels of mechanical performance particularly lower levels of fatigue resistance. Obtaining defect-free final parts therefore calls for a better understanding of how the processing parameters affect the thermal history, microstructure, and mechanical properties of LMD Ti–6Al–4V.
iii. Optimization of the processing parameters usually requires a large number of experimental tests, which may be expensive and time-consuming. Due to the large number of the processing parameters, it is a common practice to keep some of those parameters unchanged. This could speed up the optimization process but may result in systematic uncertainties. An alternative approach is the use of the computational models that consider the relevant thermo-mechanical phenomena. However, the complexity of the interactions between the shield gas, molten material, and blown powder, together with the complex regimens of heat transfer make the process very difficult to model.
iv. In general, the mechanical properties of LMD Ti–6Al–4V can be inferior, similar, or even superior to those of its wrought counterparts. If the martensitic α phase forms due to a high cooling rate, it is possible to obtain a higher strength than the wrought alloy but this increase is usually accompanied by a decrease in ductility.
v. As compared to the wrought alloy, LMD Ti–6Al–4V usually exhibits lower values of the fatigue strength and fracture toughness. The fine microstructure resulting from LMD leads to a higher level of crack initiation resistance under HCF conditions. In contrast, coarser microstructures are more resistant to crack propagation, giving rise to a more favorable LCF behavior. Usually initiating at voids or pores, the adiabatic shear bands are the typical failure mechanism in LMD Ti–6Al–4V parts.
vi. Significant levels of anisotropy have been reported for both tensile and fatigue properties of LMD Ti–6Al–4V parts. If the transversal direction is defined as the one parallel to the build axis, longitudinal specimens exhibit higher values of the tensile strength than those deposited along the transversal direction.

To date, much efforts has been made for the successful fabrication of Ti–6Al–4V components through different AM processes including LMD. Researchers often select some of the processing parameters as the main variables while leaving the others unchanged. This might limit our ability to exploit the full potential of LMD for obtaining fully dense Ti–6Al–4V parts with favorable microstructures and superior mechanical properties. There is therefore a need for complete maps that relate as many as possible processing parameters to the resulting microstructures and mechanical properties. These maps can be helpful for determining the best set of processing parameters for any given application. It is

therefore suggested that future studies should try to determine such maps.

The relationships between the processing parameters and the microstructure of the resulting materials is not yet fully understood. Further investigations are required to evaluate the influence of the grain size and orientation on the mechanical properties of the finished parts. A good control over the processing parameters and, thus, the microstructure and mechanical properties of the resulting material would pave the way for a wider commercial adoption of the LMD process. In particular, a better understanding of the role of different factors in the formation of defects such as pores and cracks is required to ensure that LMD parts meet the quality standards. Further developments in mathematical models that could describe the interactions between the laser beam and the deposited material are needed to allow us better understand the solidification behavior occurring during the LMD process. Finally, commercially available LMD systems that incorporate closed-loop control and monitoring systems could assist in further development of this important manufacturing process.References

[1] J. De Damborenea, M. Arenas, M.A. Larosa, A.L. Jardini, C.A. de Carvalho Zavaglia, A. Conde, Corrosion of Ti6Al4V pins produced by direct metal laser sintering, Appl. Surf. Sci. 393 (2017) 340–347.

[2] Q. Liu, Y. Wang, H. Zheng, K. Tang, L. Ding, H. Li, S. Gong, Microstructure and mechanical properties of LMD–SLM hybrid forming Ti6Al4V alloy, Mater. Sci. Eng. A 660 (2016) 24–33.

[3] ISO 17296-2:2015, Additive Manufacturing. General Principles. Part 2: Overview of Process Categories and Feedstock, ISO, 2015, 17296-2:2015.

[4] G. Nicoletto, Anisotropic high cycle fatigue behavior of Ti–6Al–4V obtained by powder bed laser fusion, Int. J. Fatigue 94 (2017) 255–262.

[5] S.K. Everton, M. Hirsch, P. Stravroulakis, R.K. Leach, A.T. Clare, Review of in-situ process monitoring and in-situ metrology for metal additive manufacturing, Mater. Des. 95 (2016) 431–445.

[6] S. Wolff, T. Lee, E. Faierson, K. Ehmann, J. Cao, Anisotropic properties of directed energy deposition (DED)-processed Ti–6Al–4V, J. Manuf. Process. 24 (2016) 397–405.

[7] D. Greitemeier, F. Palm, F. Syassen, T. Melz, Fatigue performance of additive manufactured TiAl6V4 using electron and laser beam melting, Int. J. Fatigue 94 (2017) 211–217.

[8] E. Fereiduni, M. Yakout, M. Elbestawi, Laser-Based Additive Manufacturing of Lightweight Metal Matrix Composites in: Additive Manufacturing of Emerging Materials, Springer, 2019, pp. 55–109.

[9] C. De Formanoir, S. Michotte, O. Rigo, L. Germain, S. Godet, Electron beam melted Ti–6Al–4V: microstructure, texture and mechanical behavior of the as-built and heat-treated material, Mater. Sci. Eng. A 652 (2016) 105–119.

[10] R. Raju, M. Duraiselvam, V. Petley, S. Verma, R. Rajendran, Microstructural and mechanical characterization of Ti6Al4V refurbished parts obtained by laser metal deposition, Mater. Sci. Eng. A 643 (2015) 64–71.

[11] B. Zhu, P. Xia, Y. Li, W. Ho, J. Yu, Fabrication and photocatalytic activity enhanced mechanism of direct Z-scheme g-C3N4/Ag2WO4 photocatalyst, Appl. Surf. Sci. 391 (2017) 175–183.

[12] A. Zadpoor, Frontiers of additively manufactured metallic materials, Materials 11 (2018) 1566–1576.

[13] E.T. Akinlabi, R.M. Mahamood, S.A. Akinlabi, Advanced Manufacturing Techniques Using Laser Material Processing, IGI Global, 2016.

[14] C. Selcuk, Laser metal deposition for powder metallurgy parts, Powder Metall. 54 (2011) 94–99.

[15] J. Vaithilingam, E. Prina, R.D. Goodridge, R.J. Hague, S. Edmondson, F.R. Rose, S.D. Christie, Surface chemistry of Ti6Al4V components fabricated using selective laser melting for biomedical applications, Mater. Sci. Eng. C 67 (2016) 294–303.

[16] B. Van Hooreweder, Y. Apers, K. Lietaert, J.-P. Kruth, Improving the fatigue performance of porous metallic biomaterials produced by Selective Laser Melting, Acta Biomater. 47 (2017) 193–202.

[17] L. Murr, S. Quinones, S. Gaytan, M. Lopez, A. Rodela, E. Martinez, D. Hernandez, E. Martinez, F. Medina, R. Wicker, Microstructure and mechanical behavior of Ti–6Al–4V produced by rapid-layer manufacturing, for biomedical applications, J. Mech. Behav. Biomed. Mater. 2 (2009) 20–32.

[18] A. Bordin, S. Sartori, S. Bruschi, A. Ghiotti, Experimental investigation on the feasibility of dry and cryogenic machining as sustainable strategies when turning Ti6Al4V produced by Additive Manufacturing, J. Clean. Prod. 142 (2017) 4142–4151.

[19] J. Vaithilingam, R.D. Goodridge, R.J. Hague, S.D. Christie, S. Edmondson, The effect of laser remelting on the surface chemistry of Ti6al4V components fabricated by selective laser melting, J. Mater. Process. Technol. 232 (2016) 1–8.

[20] S. Liu, Y.C. Shin, The influences of melting degree of TiC reinforcements on microstructure and mechanical properties of laser direct deposited Ti6Al4V-TiC composites, Mater. Des. 136 (2017) 185–195.

[21] B. Baufeld, O. Van der Biest, R. Gault, Additive manufacturing of Ti–6Al–4V components by shaped metal deposition: microstructure and mechanical properties, Mater. Des. 31 (2010) S106–S111.

[22] W. Mei, J. Sun, Y. Wen, Martensitic transformation from β to α′ and α ″phases in Ti–V alloys: a first-principles study, J. Mater. Res. 32 (2017) 3183–3190.

[23] F. Bartolomeu, M. Buciumeanu, E. Pinto, N. Alves, F. Silva, O. Carvalho, G. Miranda, Wear behavior of Ti6Al4V biomedical alloys processed by selective laser melting, hot pressing and conventional casting, Trans. Nonferr. Metal. Soc. 27 (2017) 829–838.

[24] M. Shunmugavel, A. Polishetty, G. Littlefair, Microstructure and mechanical properties of wrought and additive manufactured Ti-6Al-4 V cylindrical bars, Procedia Technol. 20 (2015) 231–236.

[25] G. Lütjering, Influence of processing on microstructure and mechanical properties of (α+ β) titanium alloys, Mater. Sci. Eng. A 243 (1998) 32–45.

[26] G. Welsch, R. Boyer, E. Collings, Materials Properties Handbook: Titanium Alloys, ASM International, 1993.

[27] S. Lampman, Wrought titanium and titanium alloys, Metal Handbook 2 (1990) 592–633.

[28] D. Clark, M.T. Whittaker, M.R. Bache, Microstructural characterization of a prototype titanium alloy structure processed via direct laser deposition (DLD), Metall. Mater. Trans. B 43 (2012) 388–396.

[29] T. Vilaro, C. Colin, J.-D. Bartout, As-fabricated and heat-treated microstructures of the Ti-6Al-4V alloy processed by selective laser melting, Metall. Mater. Trans. A 42 (2011) 3190–3199.

[30] P.-H. Li, W.-G. Guo, W.-D. Huang, Y. Su, X. Lin, K.-B. Yuan, Thermomechanical response of 3D laser-deposited Ti–6Al–4V alloy over a wide range of strain rates and temperatures, Mater. Sci. Eng. A 647 (2015) 34–42.

[31] L. Bian, S.M. Thompson, N. Shamsaei, Mechanical properties and microstructural features of direct laser-deposited Ti-6Al-4V, J. Occup. Med. 67 (2015) 629–638.

[32] X. Wang, S. Xu, S. Zhou, W. Xu, M. Leary, P. Choong, M. Qian, M. Brandt, Y.M. Xie, Topological design and additive manufacturing of porous metals for bone scaffolds and orthopaedic implants: a review, Biomaterials 83 (2016) 127–141.

[33] P. Edwards, M. Ramulu, Fatigue performance evaluation of selective laser melted Ti–6Al–4V, Mater. Sci. Eng. A 598 (2014) 327–337.

[34] A. Majorell, S. Srivatsa, R. Picu, Mechanical behavior of Ti–6Al–4V at high and moderate temperatures—Part I: experimental results, Mater. Sci. Eng., A 326 (2002) 297–305.

[35] R. Picu, A. Majorell, Mechanical behavior of Ti–6Al–4V at high and moderate temperatures—Part II: constitutive modeling, Mater. Sci. Eng., A 326 (2002) 306–316.

[36] G. Kasperovich, J. Haubrich, J. Gussone, G. Requena, Correlation between porosity and processing parameters in TiAl6V4 produced by selective laser melting, Mater. Des. 105 (2016) 160–170.

[37] V. Weißmann, R. Bader, H. Hansmann, N. Laufer, Influence of the structural orientation on the mechanical properties of selective laser melted Ti6Al4V open-porous scaffolds, Mater. Des. 95 (2016) 188–197.

[38] F. Bartolomeu, M. Sampaio, O. Carvalho, E. Pinto, N. Alves, J. Gomes, F. Silva, G. Miranda, Tribological behavior of Ti6Al4V cellular structures produced by Selective Laser Melting, J. Mech. Behav. Biomed. Mater. 69 (2017) 128–134.

[39] Y. Lv, J. Li, Y. Tao, L. Hu, Oxidation behaviors of the TiNi/Ti 2 Ni matrix composite coatings with different contents of TaC addition fabricated on Ti6Al4V by laser cladding, J. Alloy. Comp. 679 (2016) 202–212.

[40] G. Miranda, A. Araújo, F. Bartolomeu, M. Buciumeanu, O. Carvalho, J. Souza, F. Silva, B. Henriques, Design of Ti6Al4V-HA composites produced by hot pressing for biomedical applications, Mater. Des. 108 (2016) 488–493.

[41] N. Manam, W. Harun, D. Shri, S. Ghani, T. Kurniawan, M.H. Ismail, M. Ibrahim, Study of corrosion in biocompatible metals for implants: a review, J. Alloy. Comp. 701 (2017) 698–715.

[42] A.J. Sterling, B. Torries, N. Shamsaei, S.M. Thompson, D.W. Seely, Fatigue behavior and failure mechanisms of direct laser deposited Ti–6Al–4V, Mater. Sci. Eng. A 655 (2016) 100–112.

[43] S.M. Thompson, L. Bian, N. Shamsaei, A. Yadollahi, An overview of Direct Laser Deposition for additive manufacturing; Part I: transport phenomena, modeling and diagnostics, Addit. Manuf. 8 (2015) 36–62.

[44] C.O. Brown, E.M. Breinan, B.H. Kear, Method for Fabricating Articles by Sequential Layer Deposition, in, U.S. Patent, 1982.

[45] P.P. Mehta, R.R. Otten, E.B. Cooper Jr, Method and Apparatus for Repairing Metal in an Article, in, U.S. Patent, 1988.

[46] A.W. Hammeke, Laser Spray Nozzle and Method, in, U.S. Patent, 1988.

[47] A. Buongiorno, Laser/powdered metal cladding nozzle, in, U.S. Patent, 1995.

[48] G.K. Lewis, R. Nemec, J. Milewski, D.J. Thoma, D. Cremers, M. Barbe, Directed light fabrication, in: Los Alamos National Lab., NM (United States), 1994.

[49] M.N. Ahsan, A.J. Pinkerton, R.J. Moat, J. Shackleton, A comparative study of laser direct metal deposition characteristics using gas and plasma-atomized Ti–6Al–4V powders, Mater. Sci. Eng. A 528 (2011) 7648–7657.

[50] B. Baufeld, E. Brandl, O. Van der Biest, Wire based additive layer manufacturing: comparison of microstructure and mechanical properties of Ti–6Al–4V components fabricated by laser-beam deposition and shaped metal deposition, J. Mater. Process. Technol. 211 (2011) 1146–1158.

[51] B. Graf, A. Gumenyuk, M. Rethmeier, Laser metal deposition as repair technology for stainless steel and titanium alloys, Phys. Procedia 39 (2012) 376–381.
[52] H. Paydas, A. Mertens, R. Carrus, J. Lecomte-Beckers, J.T. Tchuindjang, Laser cladding as repair technology for Ti–6Al–4V alloy: influence of building strategy on microstructure and hardness, Mater. Des. 85 (2015) 497–510.
[53] A. Lundbäck, R. Pederson, M.H. Colliander, C. Brice, A. Steuwer, A. Heralic, T. Buslaps, L.E. Lindgren, Modeling and experimental measurement with synchrotron radiation of residual stresses in laser metal deposited Ti-6Al-4V, in: Proceedings of the 13th World Conference on Titanium, Wiley Online Library, 2016, pp. 1279–1282.
[54] A.J. Yule, J.J. Dunkley, Atomization of Melts for Powder Production and Spray Deposition, Oxford University Press, USA, 1994.
[55] E. Brandl, F. Palm, V. Michailov, B. Viehweger, C. Leyens, Mechanical properties of additive manufactured titanium (Ti–6Al–4V) blocks deposited by a solid-state laser and wire, Mater. Des. 32 (2011) 4665–4675.
[56] A. Segerstark, J. Andersson, L.-E. Svensson, Economical viability of laser metal deposition, in: The 6th Swedish Production Symposium, Sweden, 2014.
[57] G. Marchese, X. Garmendia Colera, F. Calignano, M. Lorusso, S. Biamino, P. Minetola, D. Manfredi, Characterization and comparison of Inconel 625 processed by selective laser melting and laser metal deposition, Adv. Eng. Mater. 19 (2017) 1–9.
[58] T. Tancogne-Dejean, C.C. Roth, U. Woy, D. Mohr, Probabilistic fracture of Ti–6Al–4V made through additive layer manufacturing, Int. J. Plast. 78 (2016) 145–172.
[59] http://www.sciaky.com/additive-manufacturing/wire-am-vs-powder-am.
[60] M. Ziętala, T. Durejko, M. Polański, I. Kunce, T. Płociński, W. Zieliński, M. Łazińska, W. Stępniowski, T. Czujko, K.J. Kurzydłowski, The microstructure, mechanical properties and corrosion resistance of 316L stainless steel fabricated using laser engineered net shaping, Mater. Sci. Eng. A 677 (2016) 1–10.
[61] J. Mazumder, A. Schifferer, J. Choi, Direct materials deposition: designed macro and microstructure, Mater. Res. Innov. 3 (1999) 118–131.
[62] J. Yang, F. Wang, 3D finite element temperature field modelling for direct laser fabrication, Int. J. Adv. Manuf. Technol. 43 (2009) 1060–1068.
[63] M. Froend, S. Riekehr, N. Kashaev, B. Klusemann, J. Enz, Process development for wire-based laser metal deposition of 5087 aluminium alloy by using fibre laser, J. Manuf. Process. 34 (2018) 721–732.
[64] D. Bourell, J.P. Kruth, M. Leu, G. Levy, D. Rosen, A.M. Beese, A. Clare, Materials for additive manufacturing, CIRP Ann. - Manuf. Technol. 66 (2017) 659–681.
[65] P. Åkerfeldt, M.-L. Antti, R. Pederson, Influence of microstructure on mechanical properties of laser metal wire-deposited Ti-6Al-4V, Mater. Sci. Eng. A 674 (2016) 428–437.
[66] A.R. Nassar, J.S. Keist, E.W. Reutzel, T.J. Spurgeon, Intra-layer closed-loop control of build plan during directed energy additive manufacturing of Ti–6Al–4V, Addit. Manuf. 6 (2015) 39–52.
[67] E. Brandl, V. Michailov, B. Viehweger, C. Leyens, Deposition of Ti–6Al–4V using laser and wire, part I: microstructural properties of single beads, Surf. Coating. Technol. 206 (2011) 1120–1129.
[68] W.E. King, H.D. Barth, V.M. Castillo, G.F. Gallegos, J.W. Gibbs, D.E. Hahn, C. Kamath, A.M. Rubenchik, Observation of keyhole-mode laser melting in laser powder-bed fusion additive manufacturing, J. Mater. Process. Technol. 214 (2014) 2915–2925.
[69] U.S. Bertoli, A.J. Wolfer, M.J. Matthews, J.-P.R. Delplanque, J.M. Schoenung, On the limitations of volumetric energy density as a design parameter for selective laser melting, Mater. Des. 113 (2017) 331–340.
[70] E.W. Reutzel, A.R. Nassar, A survey of sensing and control systems for machine and process monitoring of directed-energy, metal-based additive manufacturing, Rapid Prototyp. J. 21 (2015) 159–167.
[71] A. Nickel, D. Barnett, F. Prinz, Thermal stresses and deposition patterns in layered manufacturing, Mater. Sci. Eng. A 317 (2001) 59–64.
[72] G. Dinda, A. Dasgupta, J. Mazumder, Laser aided direct metal deposition of Inconel 625 superalloy: microstructural evolution and thermal stability, Mater. Sci. Eng. A 509 (2009) 98–104.
[73] P. Kobyrn, S. Semiatin, Mechanical properties of laser-deposited Ti-6Al-4V solid freeform fabrication symposium, in: Solid Freeform Fabrication Proceedings, Austin, USA, 2001, pp. 6–8.
[74] P. Kobryn, S. Semiatin, The laser additive manufacture of Ti-6Al-4V, J. Occup. Med. 53 (2001) 40–42.
[75] X. Wu, J. Liang, J. Mei, C. Mitchell, P. Goodwin, W. Voice, Microstructures of laser-deposited Ti–6Al–4V, Mater. Des. 25 (2004) 137–144.
[76] Y. Zhai, H. Galarraga, D.A. Lados, Microstructure, static properties, and fatigue crack growth mechanisms in Ti-6Al-4V fabricated by additive manufacturing: LENS and EBM, Eng. Fail. Anal. 69 (2016) 3–14.
[77] Y. Zhai, H. Galarraga, D.A. Lados, Microstructure evolution, tensile properties, and fatigue damage mechanisms in Ti-6Al-4V alloys fabricated by two additive manufacturing techniques, Procedia Eng. 114 (2015) 658–666.
[78] S. Kelly, S. Kampe, Microstructural evolution in laser-deposited multilayer Ti-6Al-4V builds: Part I. Microstructural characterization, Metall. Mater. Trans. A 35 (2004) 1861–1867.
[79] E. Amsterdam, G. Kool, High cycle fatigue of laser beam deposited Ti-6Al-4V and Inconel 718, in: ICAF, Springer, 2009, pp. 1261–1274.
[80] C. Qiu, G. Ravi, C. Dance, A. Ranson, S. Dilworth, M.M. Attallah, Fabrication of large Ti–6Al–4V structures by direct laser deposition, J. Alloy. Comp. 629 (2015) 351–361.
[81] S.J. Wolff, S. Lin, E.J. Faierson, W.K. Liu, G.J. Wagner, J. Cao, A framework to link localized cooling and properties of directed energy deposition (DED)-processed Ti-6Al-4V, Acta Mater. 132 (2017) 106–117.
[82] S. Wolff, T. Lee, E. Faierson, K. Ehmann, J. Cao, Anisotropic properties of directed energy deposition (DED)-processed Ti–6Al–4V, J. Manuf. Process. 24 (2016) 397–405.
[83] M.N. Ahsan, R. Bradley, A.J. Pinkerton, Microcomputed tomography analysis of intralayer porosity generation in laser direct metal deposition and its causes, J. Laser Appl. 23 (2011) 1–10.
[84] S. Hashmi, Comprehensive Materials Processing, Elsevier, 2014.
[85] Y. Zhai, H. Galarraga, D.A. Lados, Microstructure evolution, tensile properties, and fatigue damage mechanisms in Ti-6Al-4V alloys fabricated by two additive manufacturing techniques, Procedia Eng. 114 (2015) 658–666.
[86] S. Kelly, S. Kampe, Microstructural evolution in laser-deposited multilayer Ti-6Al-4V builds: Part II. Thermal modeling, Metall. Mater. Trans. A 35 (2004) 1869–1879.
[87] J. Donoghue, A. Gholinia, J.Q.d. Fonseca, P. Prangnell, In-situ high temperature EBSD analysis of the effect of a deformation step on the alpha to beta transition in additive manufactured Ti-6Al-4V, in: Proceedings of the 13th World Conference on Titanium, Wiley Online Library, 2015, pp. 1283–1288.
[88] X. Wu, J. Liang, J. Mei, C. Mitchell, P. Goodwin, W. Voice, Microstructures of laser-deposited Ti–6Al–4V, Mater. Des. 25 (2004) 137–144.
[89] T. Ahmed, H. Rack, Phase transformations during cooling in α+ β titanium alloys, Mater. Sci. Eng. A 243 (1998) 206–211.
[90] Y. Zhai, D.A. Lados, E.J. Brown, G.N. Vigilante, Understanding the microstructure and mechanical properties of Ti-6Al-4V and Inconel 718 alloys manufactured by laser engineered net shaping, Addit. Manuf. 27 (2019) 334–344.
[91] N.A. Kistler, D.J. Corbin, A.R. Nassar, E.W. Reutzel, A.M. Beese, Effect of processing conditions on the microstructure, porosity, and mechanical properties of Ti-6Al-4V repair fabricated by directed energy deposition, J. Mater. Process. Technol. 264 (2019) 172–181.
[92] G.J. Marshall, W.J. Young, S.M. Thompson, D. Seely, N. Shamsaei, Effect of substrate thickness on micro-hardness of direct laser deposited Ti-6Al-4V parts, in: 56th AIAA/ASCE/AHS/ASC Structures, Structural Dynamics, and Materials Conference, 2015, pp. 1356–1365.
[93] S.A. Khairallah, A.T. Anderson, A. Rubenchik, W.E. King, Laser powder-bed fusion additive manufacturing: physics of complex melt flow and formation mechanisms of pores, spatter, and denudation zones, Acta Mater. 108 (2016) 36–45.
[94] B.A. Szost, S. Terzi, F. Martina, D. Boisselier, A. Prytuliak, T. Pirling, M. Hofmann, D.J. Jarvis, A comparative study of additive manufacturing techniques: residual stress and microstructural analysis of CLAD and WAAM printed Ti–6Al–4V components, Mater. Des. 89 (2016) 559–567.
[95] R. Moat, A. Pinkerton, L. Li, P. Withers, M. Preuss, Residual stresses in laser direct metal deposited Waspaloy, Mater. Sci. Eng. A 528 (2011) 2288–2298.
[96] K. Zhang, S. Wang, W. Liu, R. Long, Effects of substrate preheating on the thin-wall part built by laser metal deposition shaping, Appl. Surf. Sci. 317 (2014) 839–855.
[97] S. Ghosh, J. Choi, Three-dimensional transient finite element analysis for residual stresses in the laser aided direct metal/material deposition process, J. Laser Appl. 17 (2005) 144–158.
[98] R. Moat, A. Pinkerton, L. Li, P. Withers, M. Preuss, Residual stresses in laser direct metal deposited Waspaloy, Mater. Sci. Eng. A 528 (2011) 2288–2298.
[99] S. Ghosh, J. Choi, Three-dimensional transient finite element analysis for residual stresses in the laser aided direct metal/material deposition process, J. Laser Appl. 17 (2005) 144–158.
[100] J. Zhang, F. Liou, W. Seufzer, K. Taminger, A coupled finite element cellular automaton model to predict thermal history and grain morphology of Ti-6Al-4V during direct metal deposition (DMD), Addit. Manuf. 11 (2016) 32–39.
[101] A. Sterling, N. Shamsaei, B. Torries, S.M. Thompson, Fatigue behaviour of additively manufactured Ti-6Al-4 V, Procedia Eng. 133 (2015) 576–589.
[102] N. Biswas, J. Ding, V.K. Balla, D. Field, A. Bandyopadhyay, Deformation and fracture behavior of laser processed dense and porous Ti6Al4V alloy under static and dynamic loading, Mater. Sci. Eng. A 549 (2012) 213–221.
[103] J. Heigel, P. Michaleris, E. Reutzel, Thermo-mechanical model development and validation of directed energy deposition additive manufacturing of Ti–6Al–4V, Addit. Manuf. 5 (2015) 9–19.
[104] Q. Yang, P. Zhang, L. Cheng, Z. Min, M. Chyu, A.C. To, Finite element modeling and validation of thermomechanical behavior of Ti-6Al-4V in directed energy deposition additive manufacturing, Addit. Manuf. 12 (2016) 169–177.
[105] S. Marimuthu, D. Clark, J. Allen, A. Kamara, P. Mativenga, L. Li, R. Scudamore, Finite element modelling of substrate thermal distortion in direct laser additive manufacture of an aero-engine component, Proc. Inst. Mech. Eng. Part C 227 (2013) 1987–1999.
[106] R. Ye, J.E. Smugeresky, B. Zheng, Y. Zhou, E.J. Lavernia, Numerical modeling of the thermal behavior during the LENS® process, Mater. Sci. Eng. A 428 (2006) 47–53.
[107] B. Baufeld, O. Van der Biest, Mechanical properties of Ti-6Al-4V specimens produced by shaped metal deposition, Sci. Technol. Adv. Mater. 10 (2009) 1–10.
[108] P. Åkerfeldt, M.-L. Antti, R. Pederson, Influence of microstructure on mechanical properties of laser metal wire-deposited Ti-6Al-4V, Mater. Sci. Eng. A 674 (2016) 428–437.

[109] J. Yao, T. Suo, S. Zhang, F. Zhao, H. Wang, J. Liu, Y. Chen, Y. Li, Influence of heat-treatment on the dynamic behavior of 3D laser-deposited Ti–6Al–4V alloy, Mater. Sci. Eng. A 677 (2016) 153–162.
[110] E. Brandl, A. Schoberth, C. Leyens, Morphology, microstructure, and hardness of titanium (Ti-6Al-4V) blocks deposited by wire-feed additive layer manufacturing (ALM), Mater. Sci. Eng. A 532 (2012) 295–307.
[111] N. Sridharan, A. Chaudhary, P. Nandwana, S.S. Babu, Texture evolution during laser direct metal deposition of Ti-6Al-4V, J. Occup. Med. 68 (2016) 772–777.
[112] E. Brandl, D. Greitemeier, Microstructure of additive layer manufactured Ti–6Al–4V after exceptional post heat treatments, Mater. Lett. 81 (2012) 84–87.
[113] P.-H. Li, W.-G. Guo, W.-D. Huang, Y. Su, X. Lin, K.-B. Yuan, Thermomechanical response of 3D laser-deposited Ti–6Al–4V alloy over a wide range of strain rates and temperatures, Mater. Sci. Eng. A 647 (2015) 34–42.
[114] D.L. Prakash, R. Ding, R. Moat, I. Jones, P. Withers, J.Q. da Fonseca, M. Preuss, Deformation twinning in Ti-6Al-4 V during low strain rate deformation to moderate strains at room temperature, Mater. Sci. Eng. A 527 (2010) 5734–5744.
[115] Y. Zhai, D.A. Lados, E.J. Brown, G.N. Vigilante, Fatigue crack growth behavior and microstructural mechanisms in Ti-6Al-4V manufactured by laser engineered net shaping, Int. J. Fatigue 93 (2016) 51–63.
[116] B. Baufeld, E. Brandl, O. Van der Biest, Wire based additive layer manufacturing: comparison of microstructure and mechanical properties of Ti–6Al–4V components fabricated by laser-beam deposition and shaped metal deposition, J. Mater. Process. Technol. 211 (2011) 1146–1158.
[117] J. Lin, Y. Lv, Y. Liu, B. Xu, Z. Sun, Z. Li, Y. Wu, Microstructural evolution and mechanical properties of Ti-6Al-4V wall deposited by pulsed plasma arc additive manufacturing, Mater. Des. 102 (2016) 30–40.
[118] J. Lin, Y. Lv, Y. Liu, Z. Sun, K. Wang, Z. Li, Y. Wu, B. Xu, Microstructural evolution and mechanical property of Ti-6Al-4V wall deposited by continuous plasma arc additive manufacturing without post heat treatment, J. Mech. Behav. Biomed. Mater. 69 (2017) 19–29.
[119] G. Lütjering, J.C. Williams, Alpha+ beta alloys, Titanium (2007) 203–258.
[120] US Department of Defense, Military Handbook: Titanium and Titanium Alloys, 1974.
[121] S.M. Kelly, Thermal and Microstructure Modeling of Metal Deposition Processes with Application to Ti-6Al-4V, Tech University, Virginiax, 2004. Doctoral dissertation.
[122] B.E. Carroll, T.A. Palmer, A.M. Beese, Anisotropic tensile behavior of Ti–6Al–4V components fabricated with directed energy deposition additive manufacturing, Acta Mater. 87 (2015) 309–320.
[123] J.S. Keist, T.A. Palmer, Role of geometry on properties of additively manufactured Ti-6Al-4V structures fabricated using laser based directed energy deposition, Mater. Des. 106 (2016) 482–494.
[124] J. Manero, F. Gil, J. Planell, Deformation mechanisms of Ti–6Al–4V alloy with a martensitic microstructure subjected to oligocyclic fatigue, Acta Mater. 48 (2000) 3353–3359.
[125] G.G. Yapici, I. Karaman, Z.-P. Luo, Mechanical twinning and texture evolution in severely deformed Ti–6Al–4V at high temperatures, Acta Mater. 54 (2006) 3755–3771.
[126] S. Cao, R. Chu, X. Zhou, K. Yang, Q. Jia, C.V.S. Lim, A. Huang, X. Wu, Role of martensite decomposition in tensile properties of selective laser melted Ti-6Al-4V, J. Alloy. Comp. 744 (2018) 357–363.
[127] S. Cao, Z. Chen, C.V.S. Lim, K. Yang, Q. Jia, T. Jarvis, D. Tomus, X. Wu, Defect, microstructure, and mechanical property of Ti-6Al-4V alloy fabricated by high-power selective laser melting, J. Occup. Med. 69 (2017) 2684–2692.
[128] H. Atkinson, S. Davies, Fundamental aspects of hot isostatic pressing: an overview, Metall. Mater. Trans. A 31 (2000) 2981–3000.
[129] C. Qiu, G. Ravi, C. Dance, A. Ranson, S. Dilworth, M.M. Attallah, Fabrication of large Ti–6Al–4V structures by direct laser deposition, J. Alloy. Comp. 629 (2015) 351–361.
[130] A. Prabhu, T. Vincent, A. Chaudhary, W. Zhang, S. Babu, Effect of microstructure and defects on fatigue behaviour of directed energy deposited Ti–6Al–4V, Sci. Technol. Weld. Join. 20 (2015) 659–669.
[131] J. Keist, K. Taminger, T.A. Palmer, Structure-property correlations for additively manufactured Ti-6Al-4V components produced using directed energy deposition processes, in: Proceedings of the 13th World Conference on Titanium, Wiley Online Library, 2015, pp. 1395–1400.
[132] F. Gil, J. Manero, M. Ginebra, J. Planell, The effect of cooling rate on the cyclic deformation of β-annealed Ti–6Al–4V, Mater. Sci. Eng. A 349 (2003) 150–155.
[133] E. Lorant, Effect of Microstructure on Mechanical Properties of Ti-6Al-4V Structures Made by Additive Layer Manufacturing, MSc Thesis, Cranfield University, 2010, 2010.
[134] J. Zhang, X. Wang, S. Paddea, X. Zhang, Fatigue crack propagation behaviour in wire+ arc additive manufactured Ti-6Al-4V: effects of microstructure and residual stress, Mater. Des. 90 (2016) 551–561.
[135] C. Li, B. Vrancken, M. Rombouts, J.V. Humbeeck, On the fatigue crack growth performance of Ti6Al4V manufactured by laser metal deposition, in: Proceedings of the 13th World Conference on Titanium, Wiley Online Library, 2016, pp. 1453–1457.
[136] A. Candel-Ruiz, S. Kaufmann, O. Müllerschön, Strategies for high deposition rate additive manufacturing by Laser Metal Deposition, Proceedings of lasers in manufacturing (LiM) (2015) 584–610.
[137] A. Zhang, B. Qi, B. Shi, D. Li, Effect of curvature radius on the residual stress of thin-walled parts in laser direct forming, Int. J. Adv. Manuf. Technol. 79 (2015) 81–88.
[138] J. Zhang, X. Wang, S. Paddea, X. Zhang, Fatigue crack propagation behaviour in wire+ arc additive manufactured Ti-6Al-4V: effects of microstructure and residual stress, Mater. Des. 90 (2016) 551–561.
[139] J. Beuth, N. Klingbeil, The role of process variables in laser-based direct metal solid freeform fabrication, J. Occup. Med. 53 (2001) 36–39.
[140] T. Mukherjee, V. Manvatkar, A. De, T. DebRoy, Mitigation of thermal distortion during additive manufacturing, Scripta Mater. 127 (2017) 79–83.
[141] P. Aggarangsi, J.L. Beuth, Localized preheating approaches for reducing residual stress in additive manufacturing, in: Proc. SFF Symp., Austin, 2006, pp. 709–720.
[142] G. Schajer, Y. An, Residual stress determination using cross-slitting and dual-axis ESPI, Exp. Mech. 50 (2010) 169–177.
[143] C. Knowles, T. Becker, R. Tait, Residual stress measurements and structural integrity implications for selective laser melted Ti-6Al-4V, S. Afr. J. Ind. Eng. 23 (2012) 119–129.
[144] R. Leggatt, D. Smith, S. Smith, F. Faure, Development and experimental validation of the deep hole method for residual stress measurement, J. Strain Anal. Eng. Des. 31 (1996) 177–186.
[145] A.T. DeWald, M.R. Hill, Improved data reduction for the deep-hole method of residual stress measurement, J. Strain Anal. Eng. Des. 38 (2003) 65–77.
[146] N. Rossini, M. Dassisti, K. Benyounis, A.-G. Olabi, Methods of measuring residual stresses in components, Mater. Des. 35 (2012) 572–588.
[147] I. Altpeter, G. Dobmann, M. Kröning, M. Rabung, S. Szielasko, Micro-magnetic evaluation of micro residual stresses of the IInd and IIIrd order, NDT&E Int. 42 (2009) 283–290.
[148] D.G. Bansal, M. Kirkham, P.J. Blau, Effects of combined diffusion treatments and cold working on the sliding friction and wear behavior of Ti–6Al–4V, Wear 302 (2013) 837–844.
[149] B.A. Szost, S. Terzi, F. Martina, D. Boisselier, A. Prytuliak, T. Pirling, M. Hofmann, D.J. Jarvis, A comparative study of additive manufacturing techniques: residual stress and microstructural analysis of CLAD and WAAM printed Ti–6Al–4V components, Mater. Des. 89 (2016) 559–567.
[150] Michael T. Hutchings, Aaron D. Krawitz (Eds.), Measurement of Residual and Applied Stress Using Neutron Diffraction, vol. 216, Springer Science & Business Media, 2012.
[151] L. Yan, Y. Zhang, F. Liou, A conceptual design of residual stress reduction with multiple shape laser beams in direct laser deposition, Finite Elem. Anal. Des. 144 (2018) 30–37.
[152] P. Kobryn, S. Semiatin, Mechanical properties of laser-deposited Ti-6Al-4V, in: Solid Freeform Fabrication Proceedings, Austin, 2001, pp. 6–8.
[153] L. Thijs, F. Verhaeghe, T. Craeghs, J. Van Humbeeck, J.-P. Kruth, A study of the microstructural evolution during selective laser melting of Ti–6Al–4V, Acta Mater. 58 (2010) 3303–3312.
[154] J. Alcisto, A. Enriquez, H. Garcia, S. Hinkson, T. Steelman, E. Silverman, P. Valdovino, H. Gigerenzer, J. Foyos, J. Ogren, Tensile properties and microstructures of laser-formed Ti-6Al-4V, J. Mater. Eng. Perform. 20 (2011) 203–212.
[155] T. Wang, Y. Zhu, S. Zhang, H. Tang, H. Wang, Grain morphology evolution behavior of titanium alloy components during laser melting deposition additive manufacturing, J. Alloy. Comp. 632 (2015) 505–513.
[156] E. Brandl, C. Leyens, F. Palm, Mechanical properties of additive manufactured Ti-6Al-4V using wire and powder based processes, in: IOP Conference Series: Materials Science and Engineering, vol. 26, IOP Publishing, 2011, 012004. No. 1.
[157] E. Brandl, B. Baufeld, C. Leyens, R. Gault, Additive manufactured Ti-6Al-4V using welding wire: comparison of laser and arc beam deposition and evaluation with respect to aerospace material specifications, Phys. Procedia 5 (2010) 595–606.
[158] B. Baufeld, O. van der Biest, R. Gault, K. Ridgway, Manufacturing Ti-6Al-4V components by shaped metal deposition: microstructure and mechanical properties, in: IOP Conference Series: Materials Science and Engineering, vol. 26, IOP Publishing, 2011, 012001. No. 1.
[159] E. Wycisk, C. Emmelmann, S. Siddique, F. Walther, High cycle fatigue (HCF) performance of Ti-6Al-4V alloy processed by selective laser melting, in: Adv. Mater. Res., 2013, pp. 134–139.
[160] F. Wang, S. Williams, P. Colegrove, A.A. Antonysamy, Microstructure and mechanical properties of wire and arc additive manufactured Ti-6Al-4V, Metall. Mater. Trans. A 44 (2013) 968–977.
[161] E. Brandl, Microstructural and Mechanical Properties of Additive Manufactured Titanium (Ti-6Al-4V) Using Wire: Evaluation with Respect to Additive Processes Using Powder and Aerospace Material Specifications, Shaker Verlag, 2010.
[162] L. Wang, S. Felicelli, Influence of process parameters on the phase transformation and consequent hardness induced by the LENS process, in: TMS Annual Meeting & Exhibition, 2007.
[163] B. Vrancken, L. Thijs, J.-P. Kruth, J. Van Humbeeck, Heat treatment of Ti6Al4V produced by selective laser melting: microstructure and mechanical properties, J. Alloy. Comp. 541 (2012) 177–185.
[164] P. Chandramohan, S. Bhero, F. Varachia, B.A. Obadele, P.A. Olubambi, Laser additive manufactured Ti–6Al–4V alloy: heat treatment studies, Trans. Indian Inst. Met. 71 (2018) 579–587.
[165] S. Semiatin, P. Kobryn, E. Roush, D. Furrer, T. Howson, R. Boyer, D. Chellman,

Plastic flow and microstructure evolution during thermomechanical processing of laser-deposited Ti-6Al-4V preforms, Metall. Mater. Trans. A 32 (2001) 1801–1811.
[166] Y. Xu, Y. Lu, K.L. Sundberg, J. Liang, R.D. Sisson, Effect of annealing treatments on the microstructure, mechanical properties and corrosion behavior of direct metal laser sintered Ti-6Al-4V, J. Mater. Eng. Perform. 26 (2017) 2572–2582.
[167] B. Wang, J. Li, J. Sun, X. Wang, Z. Liu, Shear localization and its related microstructural evolution in the ultrafine grained titanium processed by multi-axial compression, Mater. Sci. Eng. A 612 (2014) 227–235.
[168] X. Lin, T. Yue, H. Yang, W. Huang, Solidification behavior and the evolution of phase in laser rapid forming of graded Ti6Al4V-Rene88DT alloy, Metall. Mater. Trans. A 38 (2007) 127–137.
[169] S. Zhang, X. Lin, J. Chen, W. Huang, Effect of solution temperature and cooling rate on microstructure and mechanical properties of laser solid forming Ti-6Al-4V alloy, Chin. Optic Lett. 7 (2009) 498–501.
[170] E. Amsterdam, G. Kool, High cycle fatigue of laser beam deposited Ti-6Al-4V and Inconel 718, in: ICAF 2009, Bridging the Gap between Theory and Operational Practice, Springer, 2009, pp. 1261–1274.
[171] K. Shah, A.J. Pinkerton, A. Salman, L. Li, Effects of melt pool variables and process parameters in laser direct metal deposition of aerospace alloys, Mater. Manuf. Process. 25 (2010) 1372–1380.
[172] A.E. Wilson-Heid, Z. Wang, B. McCornac, A.M. Beese, Quantitative relationship between anisotropic strain to failure and grain morphology in additively manufactured Ti-6Al-4V, Mater. Sci. Eng. A 706 (2017) 287–294.
[173] M. Gharbi, P. Peyre, C. Gorny, M. Carin, S. Morville, P. Le Masson, D. Carron, R. Fabbro, Influence of various process conditions on surface finishes induced by the direct metal deposition laser technique on a Ti–6Al–4V alloy, J. Mater. Process. Technol. 213 (2013) 791–800.
[174] Y. Lee, G. Welsch, Young's modulus and damping of Ti-6Al-4V alloy as a function of heat treatment and oxygen concentration, Mater. Sci. Eng. A 128 (1990) 77–89.
[175] A.S. Khan, R. Kazmi, B. Farrokh, M. Zupan, Effect of oxygen content and microstructure on the thermo-mechanical response of three Ti–6Al–4V alloys: experiments and modeling over a wide range of strain-rates and temperatures, Int. J. Plast. 23 (2007) 1105–1125.
[176] J.-M. Oh, B.-G. Lee, S.-W. Cho, S.-W. Lee, G.-S. Choi, J.-W. Lim, Oxygen effects on the mechanical properties and lattice strain of Ti and Ti-6Al-4V, Met. Mater. Int. 17 (2011) 733–736.
[177] S. Gao, Y. Zhang, L. Shi, B. Du, M. Xi, H. Ji, Research on laser direct deposition process of Ti-6Al-4V alloy, Acta Metall. Sin. 20 (2007) 171–180.
[178] J. Kummailil, C. Sammarco, D. Skinner, C.A. Brown, K. Rong, Effect of select LENS™ processing parameters on the deposition of Ti-6Al-4V, J. Manuf. Process. 7 (2005) 42–50.
[179] L.J. Kumar, G.K. Nair, Laser metal deposition repair applications for Ti-6Al-4V alloy, Mech. Mater. Sci. Eng. 7 (2017) 1–11.
[180] S.H. Mok, G. Bi, J. Folkes, I. Pashby, Deposition of Ti–6Al–4V using a high power diode laser and wire, Part I: investigation on the process characteristics, Surf. Coating. Technol. 202 (2008) 3933–3939.
[181] E. Brandl, V. Michailov, B. Viehweger, C. Leyens, Deposition of Ti–6Al–4V using laser and wire, part II: hardness and dimensions of single beads, Surf. Coating. Technol. 206 (2011) 1130–1141.
[182] R.M. Mahamood, E.T. Akinlabi, Scanning speed influence on the microstructure and micro hardness properties of titanium alloy produced by laser metal deposition process, Mater. Today:. Proc. 4 (2017) 5206–5214.
[183] M. Hedges, N. Calder, Near net shape rapid manufacture & repair by LENS, in: Cost Effective Manufacture via Net-Shape Processing, 2006, pp. 1–14.
[184] N.K. Dey, Additive Manufacturing Laser Deposition of Ti-6Al-4V for Aerospace Repair Application, Masters Thesis, 2014, http://scholarsmine.mst.edu/masters_theses/7295/.
[185] https://3dprint.com/229935/beam-and-pfw-aerospace-work-together/.
[186] E. Sallica-Leva, R. Caram, A. Jardini, J. Fogagnolo, Ductility improvement due to martensite α′ decomposition in porous Ti–6Al–4V parts produced by selective laser melting for orthopedic implants, J. Mech. Behav. Biomed. Mater. 54 (2016) 149–158.
[187] P. Heinl, L. Müller, C. Körner, R.F. Singer, F.A. Müller, Cellular Ti–6Al–4V structures with interconnected macro porosity for bone implants fabricated by selective electron beam melting, Acta Biomater. 4 (2008) 1536–1544.
[188] A. Ataee, Y. Li, D. Fraser, G. Song, C. Wen, Anisotropic Ti-6Al-4V gyroid scaffolds manufactured by electron beam melting (EBM) for bone implant applications, Mater. Des. 137 (2018) 345–354.
[189] G. Dinda, L. Song, J. Mazumder, Fabrication of Ti-6Al-4V scaffolds by direct metal deposition, Metall. Mater. Trans. A 39 (2008) 2914–2922.
[190] S. Van Bael, Y.C. Chai, S. Truscello, M. Moesen, G. Kerckhofs, H. Van Oosterwyck, J.-P. Kruth, J. Schrooten, The effect of pore geometry on the in vitro biological behavior of human periosteum-derived cells seeded on selective laser-melted Ti6Al4V bone scaffolds, Acta Biomater. 8 (2012) 2824–2834.
[191] A.A. Zadpoor, Bone tissue regeneration: the role of scaffold geometry, Biomater. Sci. 3 (2015) 231–245.
[192] D.W. Hutmacher, Scaffolds in tissue engineering bone and cartilage, in: The Biomaterials: Silver Jubilee Compendium, Elsevier, 2000, pp. 175–189.
[193] X. Liu, S. Wu, K.W. Yeung, Y. Chan, T. Hu, Z. Xu, X. Liu, J.C. Chung, K.M. Cheung, P.K. Chu, Relationship between osseointegration and superelastic biomechanics in porous NiTi scaffolds, Biomaterials 32 (2011) 330–338.
[194] I.A. van Hengel, M. Riool, L.E. Fratila-Apachitei, J. Witte-Bouma, E. Farrell, A.A. Zadpoor, S.A. Zaat, I. Apachitei, Selective laser melting porous metallic implants with immobilized silver nanoparticles kill and prevent biofilm formation by methicillin-resistant Staphylococcus aureus, Biomaterials 140 (2017) 1–15.
[195] S. Bakhshandeh, Z. Gorgin Karaji, K. Lietaert, A.C. Fluit, C. Boel, H.C. Vogely, T. Vermonden, W.E. Hennink, H. Weinans, A.A. Zadpoor, Simultaneous delivery of multiple antibacterial agents from additively manufactured porous biomaterials to fully eradicate planktonic and adherent Staphylococcus aureus, ACS Appl. Mater. Interfaces 9 (2017) 25691–25699.
[196] Z. Gorgin Karaji, M. Speirs, S. Dadbakhsh, J.-P. Kruth, H. Weinans, A. Zadpoor, S. Amin Yavari, Additively manufactured and surface biofunctionalized porous nitinol, ACS Appl. Mater. Interfaces 9 (2017) 1293–1304.
[197] C. Chu, G. Graf, D.W. Rosen, Design for additive manufacturing of cellular structures, Comput.-Aided Des. Applic. 5 (2008) 686–696.
[198] G. Dong, Y. Tang, Y.F. Zhao, A survey of modeling of lattice structures fabricated by additive manufacturing, J. Mech. Des. 139 (2017) 100906–100919.
[199] B.V. Krishna, W. Xue, S. Bose, A. Bandyopadhyay, Functionally graded Co–Cr–Mo coating on Ti–6Al–4V alloy structures, Acta Biomater. 4 (2008) 697–706.
[200] P. Zhang, J. Toman, Y. Yu, E. Biyikli, M. Kirca, M. Chmielus, A.C. To, Efficient design-optimization of variable-density hexagonal cellular structure by additive manufacturing: theory and validation, J. Manuf. Sci. Eng. 137 (2015), 021004.
[201] D. Brackett, I. Ashcroft, R. Hague, Topology optimization for additive manufacturing, in: Proceedings of the Solid Freeform Fabrication Symposium, Austin, TX, S, 2011, pp. 348–362.
[202] E. Garner, H.M. Kolken, C.C. Wang, A.A. Zadpoor, J. Wu, Compatibility in microstructural optimization for additive manufacturing, Addit. Manuf. 26 (2019) 65–75.
[203] G. Savio, R. Meneghello, G. Concheri, Geometric modeling of lattice structures for additive manufacturing, Rapid Prototyp. J. 24 (2018) 351–360.
[204] I. Gibson, M.F. Ashby, The mechanics of three-dimensional cellular materials, Proceedings of the Royal Society of London. A. Mathematical and Physical Sciences 382 (1982) 43–59.
[205] L. Yuan, S. Ding, C. Wen, Additive manufacturing technology for porous metal implant applications and triple minimal surface structures: a review, Bioact. Mater. 4 (2019) 56–70.
[206] A.A. Zadpoor, J. Malda, Additive manufacturing of biomaterials, tissues, and organs, Ann. Biomed. Eng. 45 (2017) 1–11.
[207] A. Zadpoor, Design for additive bio-manufacturing: from patient-specific medical devices to rationally designed meta-biomaterials, Int. J. Mol. Sci. 18 (2017) 1607.
[208] W. Harun, N. Manam, M. Kamariah, S. Sharif, A. Zulkifly, I. Ahmad, H. Miura, A review of powdered additive manufacturing techniques for Ti-6Al-4V biomedical applications, Powder Technol. (2018).
[209] S.A. Yavari, R. Wauthlé, J. van der Stok, A. Riemslag, M. Janssen, M. Mulier, J.-P. Kruth, J. Schrooten, H. Weinans, A.A. Zadpoor, Fatigue behavior of porous biomaterials manufactured using selective laser melting, Mater. Sci. Eng. C 33 (2013) 4849–4858.
[210] A. Zadpoor, Current trends in metallic orthopedic biomaterials: from additive manufacturing to bio-functionalization, infection prevention, and beyond, Int. J. Mol. Sci. 19 (2018) 2684–2694.
[211] F. Matassi, A. Botti, L. Sirleo, C. Carulli, M. Innocenti, Porous metal for orthopedics implants, Clin Cases Miner Bone Metab 10 (2013) 111–115.
[212] G. Ryan, A. Pandit, D.P. Apatsidis, Fabrication methods of porous metals for use in orthopaedic applications, Biomaterials 27 (2006) 2651–2670.
[213] M. Niinomi, Recent metallic materials for biomedical applications, Me Metall. Mater. Trans. A 33 (2002) 477–486.
[214] C.N. Kelly, N.T. Evans, C.W. Irvin, S.C. Chapman, K. Gall, D.L. Safranski, The effect of surface topography and porosity on the tensile fatigue of 3D printed Ti-6Al-4V fabricated by selective laser melting, Mater. Sci. Eng. C 98 (2019) 726–736.
[215] T. Laoui, E. Santos, K. Osakada, M. Shiomi, M. Morita, S. Shaik, N. Tolochko, F. Abe, M. Takahashi, Properties of titanium dental implant models made by laser processing, Proceedings of the Institution of Mechanical Engineers, Part. Char.: J. Mech. Eng. Sci. 220 (2006) 857–863.
[216] K. Lietaert, A. Cutolo, D. Boey, B. Van Hooreweder, Fatigue life of additively manufactured Ti6Al4V scaffolds under tension-tension, tension-compression and compression-compression fatigue load, Sci. Rep. 8 (2018) 4957–4966.
[217] Q. Ran, W. Yang, Y. Hu, X. Shen, Y. Yu, Y. Xiang, K. Cai, Osteogenesis of 3D printed porous Ti6Al4V implants with different pore sizes, J. Mech. Behav. Biomed. Mater. 84 (2018) 1–11.
[218] O.L. Harrysson, O. Cansizoglu, D.J. Marcellin-Little, D.R. Cormier, H.A. West II, Direct metal fabrication of titanium implants with tailored materials and mechanical properties using electron beam melting technology, Mater. Sci. Eng. C 28 (2008) 366–373.
[219] P. Li, D. Warner, A. Fatemi, N. Phan, Critical assessment of the fatigue performance of additively manufactured Ti–6Al–4V and perspective for future research, Int. J. Fatigue 85 (2016) 130–143.
[220] S.L. Sing, J. An, W.Y. Yeong, F.E. Wiria, Laser and electron-beam powder-bed additive manufacturing of metallic implants: a review on processes, materials and designs, J. Orthop. Res. 34 (2016) 369–385.
[221] A. Bandyopadhyay, F. Espana, V.K. Balla, S. Bose, Y. Ohgami, N.M. Davies,

Influence of porosity on mechanical properties and in vivo response of Ti6Al4V implants, Acta Biomater. 6 (2010) 1640–1648.
[222] A. Vance, K. Bari, A. Arjunan, Compressive performance of an arbitrary stiffness matched anatomical Ti64 implant manufactured using Direct Metal Laser Sintering, Mater. Des. 160 (2018) 1281–1294.
[223] J. Edgar, S. Tint, Additive manufacturing technologies: 3D printing, rapid prototyping, and direct digital manufacturing, Johnson Matthey Technol. Rev. 59 (2015) 193–198.
[224] I. Gibson, D.W. Rosen, B. Stucker, Additive Manufacturing Technologies, Springer, 2014.
[225] O.A. Mohamed, S.H. Masood, J.L. Bhowmik, Optimization of fused deposition modeling process parameters: a review of current research and future prospects, Adv. Manuf. 3 (2015) 42–53.
[226] T.D. Ngo, A. Kashani, G. Imbalzano, K.T. Nguyen, D. Hui, Additive manufacturing (3D printing): a review of materials, methods, applications and challenges, Composites Part B 143 (2018) 172–196.
[227] S.A. Tofail, E.P. Koumoulos, A. Bandyopadhyay, S. Bose, L. O'Donoghue, C. Charitidis, Additive manufacturing: scientific and technological challenges, market uptake and opportunities, Mater. Today 21 (2018) 22–37.
[228] N. Engheta, R.W. Ziolkowski, Metamaterials: Physics and Engineering Explorations, John Wiley & Sons, US, 2006.
[229] J.U. Surjadi, L. Gao, H. Du, X. Li, X. Xiong, N.X. Fang, Y. Lu, Mechanical metamaterials and their engineering applications, Adv. Eng. Mater. (2019).
[230] A.A. Zadpoor, Mechanical meta-materials, Mater. Horiz. 3 (2016) 371–381.
[231] R. Lakes, Foam structures with a negative Poisson's ratio, Science 235 (1987) 1038–1041.
[232] R. Lakes, Advances in negative Poisson's ratio materials, Adv. Mater. 5 (1993) 293–296.
[233] K.K. Dudek, D. Attard, R. Caruana-Gauci, K.W. Wojciechowski, J.N. Grima, Unimode metamaterials exhibiting negative linear compressibility and negative thermal expansion, Smart Mater. Struct. 25 (2016) 1–9.
[234] Q. Wang, J.A. Jackson, Q. Ge, J.B. Hopkins, C.M. Spadaccini, N.X. Fang, Lightweight mechanical metamaterials with tunable negative thermal expansion, Phys. Rev. Lett. 117 (2016) 175901–175907.
[235] C. Shen, J. Xu, N.X. Fang, Y. Jing, Anisotropic complementary acoustic metamaterial for canceling out aberrating layers, Phys. Rev. X 4 (2014) 1–7.
[236] L. Zigoneanu, B.-I. Popa, S.A. Cummer, Three-dimensional broadband omnidirectional acoustic ground cloak, Nat. Mater. 13 (2014) 352–355.
[237] R. Hedayati, M. Mirzaali, L. Vergani, A. Zadpoor, Action-at-a-distance metamaterials: distributed local actuation through far-field global forces, Apl. Mater. 6 (2018) 1–8.
[238] M. Mirzaali, A. Caracciolo, H. Pahlavani, S. Janbaz, L. Vergani, A. Zadpoor, Multi-material 3D printed mechanical metamaterials: rational design of elastic properties through spatial distribution of hard and soft phases, Appl. Phys. Lett. 113 (2018) 1–5.
[239] M. Mirzaali, R. Hedayati, P. Vena, L. Vergani, M. Strano, A. Zadpoor, Rational design of soft mechanical metamaterials: independent tailoring of elastic properties with randomness, Appl. Phys. Lett. 111 (2017) 1–5.
[240] M. Mirzaali, S. Janbaz, M. Strano, L. Vergani, A. Zadpoor, Shape-matching soft mechanical metamaterials, Sci. Rep. 8 (2018) 1–7.
[241] Y. Ding, M. Akbari, X.-L. Gao, L. Ai, R. Kovacevic, 3 Use of powder-feed metal additive manufacturing system for fabricating metallic metamaterials, in: Manufacturing Techniques for Materials: Engineering and Engineered, CRC Press, 2018, pp. 51–65.
[242] X. Zheng, W. Smith, J. Jackson, B. Moran, H. Cui, D. Chen, J. Ye, N. Fang, N. Rodriguez, T. Weisgraber, Multiscale metallic metamaterials, Nat. Mater. 15 (2016) 1100–1106.
[243] P. Baranowski, P. Płatek, A. Antolak-Dudka, M. Sarzyński, M. Kucewicz, T. Durejko, J. Małachowski, J. Janiszewski, T. Czujko, Deformation of honeycomb cellular structures manufactured with Laser Engineered Net Shaping (LENS) technology under quasi-static loading: experimental testing and simulation, Addit. Manuf. 25 (2019) 307–316.
[244] R. Hedayati, A. Leeflang, A. Zadpoor, Additively manufactured metallic pentamode meta-materials, Appl. Phys. Lett. 110 (2017) 1–5.
[245] D. Gu, F. Chang, D. Dai, Selective laser melting additive manufacturing of novel aluminum based composites with multiple reinforcing phases, J. Manuf. Sci. Eng. 137 (2015) 1–11.
[246] H. Xu, D. Pasini, Structurally efficient three-dimensional metamaterials with controllable thermal expansion, Sci. Rep. 6 (2016) 1–8.
[247] M.L. Griffith, L.D. Harwell, J.T. Romero, E. Schlienger, C.L. Atwood, J.E. Smugeresky, Multi-material processing by LENS, in: International Solid Freeform Fabrication Symposium, Austin, US, 1997.
[248] M. Benedetti, M. Cazzolli, V. Fontanari, M. Leoni, Fatigue limit of Ti6Al4V alloy produced by selective laser sintering, Procedia Struct. Integrity 2 (2016) 3158–3167.
[249] A. Palmquist, F.A. Shah, L. Emanuelsson, O. Omar, F. Suska, A technique for evaluating bone ingrowth into 3D printed, porous Ti6Al4V implants accurately using X-ray micro-computed tomography and histomorphometry, Micron 94 (2017) 1–8.
[250] M.B. Bezuidenhout, A.D. van Staden, G.A. Oosthuizen, D.M. Dimitrov, L.M. Dicks, Delivery of antibiotics from cementless titanium-alloy cubes may be a novel way to control postoperative infections, BioMed Res. Int. 2015 (2015) 1–7.
[251] K. Pataky, T. Braschler, A. Negro, P. Renaud, M.P. Lutolf, J. Brugger, Microdrop printing of hydrogel bioinks into 3D tissue-like geometries, Adv. Mater. 24 (2012) 391–396.
[252] S. Khademzadeh, S. Carmignato, N. Parvin, F. Zanini, P.F. Bariani, Micro porosity analysis in additive manufactured NiTi parts using micro computed tomography and electron microscopy, Mater. Des. 90 (2016) 745–752.
[253] J.O. Milewski, D.J. Thoma, J.C. Fonseca, G.K. Lewis, Development of a near net shape processing method for rhenium using directed light fabrication, Mater. Manuf. Process. 13 (1998) 719–730.
[254] M. Jovanović, S. Tadić, S. Zec, Z. Mišković, I. Bobić, The effect of annealing temperatures and cooling rates on microstructure and mechanical properties of investment cast Ti–6Al–4V alloy, Mater. Des. 27 (2006) 192–199.
[255] W.-F. Ho, A comparison of tensile properties and corrosion behavior of cast Ti–7.5 Mo with cp Ti, Ti–15Mo and Ti–6Al–4V alloys, J. Alloy. Comp. 464 (2008) 580–583.
[256] I. Sen, S. Tamirisakandala, D. Miracle, U. Ramamurty, Microstructural effects on the mechanical behavior of B-modified Ti–6Al–4V alloys, Acta Mater. 55 (2007) 4983–4993.
[257] T. Aoki, I. Okafor, I. Watanabe, M. Hattori, Y. Oda, T. Okabe, Mechanical properties of cast Ti-6Al-4V-XCu alloys, J. Oral Rehabil. 31 (2004) 1109–1114.
[258] R. Guo, L. Xu, J. Wu, R. Yang, B.Y. Zong, Microstructural evolution and mechanical properties of powder metallurgy Ti–6Al–4V alloy based on heat response, Mater. Sci. Eng. A 639 (2015) 327–334.
[259] J.D. Paramore, Z.Z. Fang, P. Sun, M. Koopman, K.R. Chandran, M. Dunstan, A powder metallurgy method for manufacturing Ti-6Al-4V with wrought-like microstructures and mechanical properties via hydrogen sintering and phase transformation (HSPT), Scripta Mater. 107 (2015) 103–106.
[260] G. Lütjering, J.C. Williams, in: Titanium, Engineering Materials and Process, Springer, 2003.
[261] J. Günther, D. Krewerth, T. Lippmann, S. Leuders, T. Tröster, A. Weidner, H. Biermann, T. Niendorf, Fatigue life of additively manufactured Ti–6Al–4V in the very high cycle fatigue regime, Int. J. Fatigue 94 (2017) 236–245.
[262] J. Günther, S. Leuders, T. Tröster, A. Weidner, H. Biermann, T. Niendorf, Fatigue Behavior of Ti-6Al-4V Additively Manufactured by Selective Laser and Electron Beam Melting–On the Impact of the Chemical Composition, Process-Induced Porosity and Surface Roughness, German Association for Materials Research and Testing, 2017, pp. 89–98.
[263] B. Vayssette, N. Saintier, C. Brugger, M. Elmay, E. Pessard, Surface roughness of Ti-6Al-4V parts obtained by SLM and EBM: effect on the high cycle fatigue life, Procedia Eng. 213 (2018) 89–97.
[264] C.-W. Lin, C.-P. Ju, J.-H.C. Lin, A comparison of the fatigue behavior of cast Ti–7.5 Mo with cp titanium, Ti–6Al–4V and Ti–13Nb–13Zr alloys, Biomaterials 26 (2005) 2899–2907.
[265] A. Dekhtyar, B. Mordyuk, D. Savvakin, V. Bondarchuk, I. Moiseeva, N. Khripta, Enhanced fatigue behavior of powder metallurgy Ti–6Al–4V alloy by applying ultrasonic impact treatment, Mater. Sci. Eng. A 641 (2015) 348–359.
[266] T. Horiya, T. Yamazaki, K. Takahashi, H. Fujii, Elimination of surface porosity in Ti-6Al-4V alloy powder compacts, Nippon Steel Tech. Rep. 62 (1994) 92–97.
[267] O. Ivasishin, K. Bondareva, V. Bondarchuk, O. Gerasimchuk, D. Savvakin, B. Gryaznov, Fatigue resistance of powder metallurgy Ti–6Al–4V alloy, Strength Mater. 36 (2004) 225–230.
[268] N. Hrabe, T. Gnäupel-Herold, T. Quinn, Fatigue properties of a titanium alloy (Ti–6Al–4V) fabricated via electron beam melting (EBM): effects of internal defects and residual stress, Int. J. Fatigue 94 (2017) 202–210.
[269] A.H. Chern, P. Nandwana, T. Yuan, M.M. Kirka, R.R. Dehoff, P.K. Liaw, C.E. Duty, A review on the fatigue behavior of Ti-6Al-4V fabricated by electron beam melting additive manufacturing, Int. J. Fatigue 119 (2019) 173–184.